Registration of 3D Ultrasound Volumes with Applications in Neurosurgery and Prostate Radiotherapy

Hang Zhou

A Thesis

in

The Department

of

Electrical and Computer Engineering

Presented in Partial Fulfillment of the Requirements

for the Degree of Master of Applied Science at

Concordia University

Montréal, Québec, Canada

December 2016

CONCORDIA UNIVERSITY

SCHOOL OF GRADUATE STUDIES

This is to certify that the thesis prepared

By: Hang Zhou

Entitled: Registration of 3D Ultrasound Volumes with Applications in Neurosurgery and Prostate Radiotherapy

and submitted in partial fulfilment of the requirements for the degree of

Master of Applied Science

Complies with the regulations of this University and meets the accepted standards with respect to originality and quality.

Signed by the final examining committee:

_____ Dr. R. Raut, Chair

_____ Dr. A. Ben Hamza (CIISE), External Examiner

_____ Dr. M. O. Ahmad, Examiner

_____ Dr. H. Rivaz, Supervisor

Approved by: _____

Dr. W. E. Lynch
Chair, Department of Electrical and Computer Engineering

_____ 20 _____

Dr. C. W. Trueman
Interim Dean, Faculty of Engineering and Computer Science

ABSTRACT

Registration of 3D Ultrasound Volumes with Applications in Neurosurgery and Prostate Radiotherapy

Hang Zhou

Brain tissue deforms significantly after opening the dura and during tumor resection, invalidating pre-operative imaging data. Ultrasound is a popular imaging modality for providing the neurosurgeon with real-time updated images of brain tissue. Interpretation of post-resection ultrasound images is difficult due to large brain shift and tissue resection. Furthermore, several factors degrade the quality of post-resection ultrasound images such as strong reflection of waves at the interface of saline water and brain tissue in resection cavities, air bubbles and the application of blood-clotting agents around the edges of resection. Image registration allows comparison of post-resection ultrasound images with higher quality pre-resection images, assists in interpretation of post-resection images and may help identify residual tumor, and as such, is of significant clinical importance. Prostate motion is known to reduce the precision of prostate radiotherapy. This motion can be categorized into intrafraction and interfraction. Interfraction motion introduces large systematic errors into the treatment and is the largest contributor to prostate planning treatment volume (PTV) margins. Conventional solutions to interfraction motion all have respective drawbacks. Clarity Autoscan system provides continuous ultrasound imaging of the prostate for interfraction motion correction, however it

is time-consuming and can have large interobserver errors. The intension of accurately targeting the prostate and reducing the side effects in treatment requests a faster and more accurate registration framework for interfraction motion correction.

In this thesis, we first propose a registration framework called Nonrigid Symmetric Registration (NSR) for accurate alignment of pre- and post-resection volumetric ultrasound images in near real-time. An outlier detection algorithm is proposed and utilized in this framework to identify non-corresponding regions (outliers) and therefore improve the robustness and accuracy of registration. We use an Efficient Second-order Minimization (ESM) method for fast and robust optimization. A symmetric and inverse-consistent method is exploited to generate realistic deformation fields. The results show that NSR significantly improves the quality of alignment between pre- and post-resection ultrasound images. Then based on this framework, we develop a rigid registration framework called Prostate Registration Framework (PRF) for alignment of the prosate region in simulation and treatment volumes. PRF is trained using 2 3D transperineal ultrasound (TPUS) images of an ultrasound prostate phantom and 20 3D TPUS images from 11 patients receiving Clarity Autoscan. Algorithm performance is evaluated using further 21 TPUS images from a total of 8 patients by comparison of the PRF with manual matching of landmarks and Clarity-based estimation of interfraction motion performed by three observers. The results show that PRF outputs more accurate alignment of the prosate region in simulation and treatment volumes than Clarity, and further, provides the reposition of the prostate in treatment images efficiently and accurately.

ACKNOWLEDGEMENTS

I would first like to thank my supervisor Dr. Hassan Rivaz of Electrical and Computer Engineering at Concordia University. The door to Prof. Rivaz's office was always open whenever I ran into a trouble spot or had a question about my research or writing. He consistently allowed research to be my own work, but steered me in the right direction whenever he thought I needed it. Without his patience and direction, I would not finish my neurosurgery project and publish my first journal.

I would also like to thank Dr. Emma Harris of the Institute of Cancer Research, who was involved in my second project. Without her participation and guidance, I would not have the opportunity to learn the knowledge of prostate radiotherapy and develop an automatic registration framework for radiotherapy treatment.

I would also like to thank Dr. Rabin Raut, Dr. Abdessamad Ben Hamza and Dr. M. Omair Ahmad who are the examiners of my thesis. I am extremely grateful and indebted to them for their sincere and valuable guidance and encouragement to me.

Finally, I must express my very profound gratitude to my parents and to my friends for providing me with unfailing support and continuous encouragement throughout my years of study and through the process of research and writing this thesis. This accomplishment would

not have been possible without them. Thank you.

This work has been supported by the Natural Sciences and Engineering Research Council of Canada (NSERC) under grants RGPIN-2015-04136.

TABLE OF CONTENTS

LIST OF TABLES

LIST OF FIGURES

LIST OF ABBREVIATIONS AND SYMBOLS

AP	Anterior-posterior
CBCT	Cone-beam CT
CT	Computed tomography
EM	Expectation maximization
ESM	Efficient second-order minimization
FM	Fiducial marker
GTR	Gross-total resection
LM	Landmark
LR	Left-right
MI	Mutual information
MRI	Magnetic resonance imaging
mTRE	Mean target registration errors
NCC	Normalized cross correlation
NSR	Non-rigid symmetric registration
PRF	Prostate registration framework
PTV	Planning treatment volume
RPV	Reference position volume
SGD	Steepest gradient descent

SI	Superior-inferior
SNR	Signal to noise ratio
SSD	Sum of squared difference
TAUS	Transabdominal ultrasound
TPUS	Transperineal ultrasound
US	Ultrasound
3D	3-dimensional

$\mathbf{T_1}$ and $\mathbf{T_2}$	Forward and backward transformations
$\mathbf{T_1} \circ \mathbf{T_2}$	Composition of forward and backward transformations
$\mathbf{V_1}$ and $\mathbf{V_2}$	Pre- and post-resection ultrasound volumes
$\mathbf{x} \subset R_d$	Glocal coordinate
$\mathbf{T_u}(\mathbf{x}) = \mathbf{x} + \mathbf{u}$	Transformation formula
$\mathbf{u_1}$	Deformation field from $\mathbf{V_1}$ to $\mathbf{V_2}$
$\mathbf{u_2}$	Deformation field from $\mathbf{V_2}$ to $\mathbf{V_1}$
D	Dissimilarity metric
$\mathbf{V_1}(\mathbf{T}_{\mathbf{u_1}(0.5)}(\mathbf{x}))$	Middle volume from $\mathbf{V_1}$
$\mathbf{V_2}(\mathbf{T}_{\mathbf{u_2}(0.5)}(\mathbf{x}))$	Middle volume from $\mathbf{V_2}$
α	Regularization weight
tr	Trace operator

$\mathrm{tr}(\nabla \mathbf{u}^T \nabla \mathbf{u})^2$	Diffusion regularization term
$\mathbf{V_{1}}_i$ and $\mathbf{V_{2}}_i$	Patch i in $\mathbf{V_1}$ and $\mathbf{V_2}$ respectively
V_{1j} and V_{2j}	Intensity of pixel j in patch i
$\overline{\mathbf{V_{1}}_i}$ and $\overline{\mathbf{V_{2}}_i}$	Mean intensity of patch i
N	Number of patches in the volume
n	Number of pixels in each patch
r	Defined metric for outlier detection
β	Coefficient for metric r
$\mathbf{std}(\mathbf{v})$	Standard deviation of the elements in vector $\mathbf{v}$
ρ_i	NCC of patch i
$\frac{\partial \rho_i}{\partial \mathbf{I}}$	Derivative vector of NCC with respect to the intensity of each pixel in patch i
$\mathbf{P}$	Defined vector for NCC
ρ_j	NCC value computed at pixel j
M	Total number of voxels in the volume
$\frac{\partial \mathbf{P}}{\partial \mathbf{I}}$	Defined vector for derivative
$\frac{\partial \rho_j}{\partial I_j}$	Derivative of NCC in pixel j with respect to the intensity of that pixel
$\frac{\partial \mathbf{I_V}}{\partial \mathbf{u}}$	Gradient of intensity
$\nabla_{\mathbf{u_1}}$ and $\nabla_{\mathbf{u_2}}$	Jacobians with respect to forward and backward deformation fields respectively
$\nabla_{\mathbf{u}} \mathbf{P_{av}}$	Average Jacobian for forward and backward deformations

$\mathbf{I}$	Identity matrix
$\nabla^2\mathbf{u}_{\mathbf{previous}}$	Laplacian of the sum of all previous updates
$\mathbf{\Delta_u}$	Incremental update
λ	Step size
$\mathbf{x}$ and $\mathbf{x}'$	Corresponding landmarks in $\mathbf{V_1}$ and $\mathbf{V_2}$ respectively
l	Number of landmarks
$\mathbf{V_s}$	Simulation TPUS image
$\mathbf{V_t}$	Treatment TPUS image
$\mathbf{V_p}$	Prostate template
$\mathbf{P_{position}}$	Position matrix of $\mathbf{V_p}$
Px, Py, Pz	Coordinates of the vertex of $\mathbf{V_p}$ in $\mathbf{V_s}$
R	Half of the search range
$\mathbf{V_{pi}}$ and $\mathbf{V_{ti}}$	Patch $\mathbf{i}$ in $\mathbf{V_p}$ and $\mathbf{V_t}$
$\mathbf{V_{pi}}_j$ and $\mathbf{V_{ti}}_j$	Intensity of pixel j in patch $\mathbf{i}$
$\overline{\mathbf{V_{pi}}}$ and $\overline{\mathbf{V_{ti}}}$	Mean intensity of patch $\mathbf{i}$
$\mathbf{T_{position}}$	Position matrix of the vertex of the corresponding region in $\mathbf{V_t}$
$\mathbf{D_{rigid}}$	Rigid deformation field from $\mathbf{V_p}$ to $\mathbf{V_t}$

Chapter 1

Introduction

In this chapter, we will first review ultrasound (US) imaging and outline its principals. We then overview image registration technique and provide some fundamental knowledge and background of our previous work.

1.1 Ultrasound imaging

US refers to the acoustic wave with the frequency over the threshold of human hearing (20kHz). It has been widely used in many areas because of its high-frequency characteristic, such as metal detection, workpiece cleaning, medical imaging and so on. In this thesis, we only focus on the application of US in medical imaging, and Fig. 1.1 shows an example of US images. The frequency of US waves normally ranges from 1 to 18 megahertz in US imaging, depending on the purpose of the imaging technology. Lower frequencies generally transmit

deeper into tissue, whereas higher frequencies are easier to reflect or scatter because of their shorter wavelength.

Figure 1.1: US image of the brain.

US waves are generated from a transducer probe with the principle of piezoelectric (pressure electricity) effect. Inside the probe, there are a few piezoelectric crystals. When they are triggered electrically, which normally caused by pressure, strong, short electrical pulses will be produced from the US machine. The waves propagate into tissue, while some of them are reflected at numerous interfaces because of the variation of acoustic impedance of different tissue types. Finally the reflected waves hit the piezoelectric crystals and are converted to

electrical currents, which are possessed into digital images in an ultrasonic scanner. Fig. 1.2 shows a GE Vivid E9 US machine and the probe where US waves are transmitted and received.

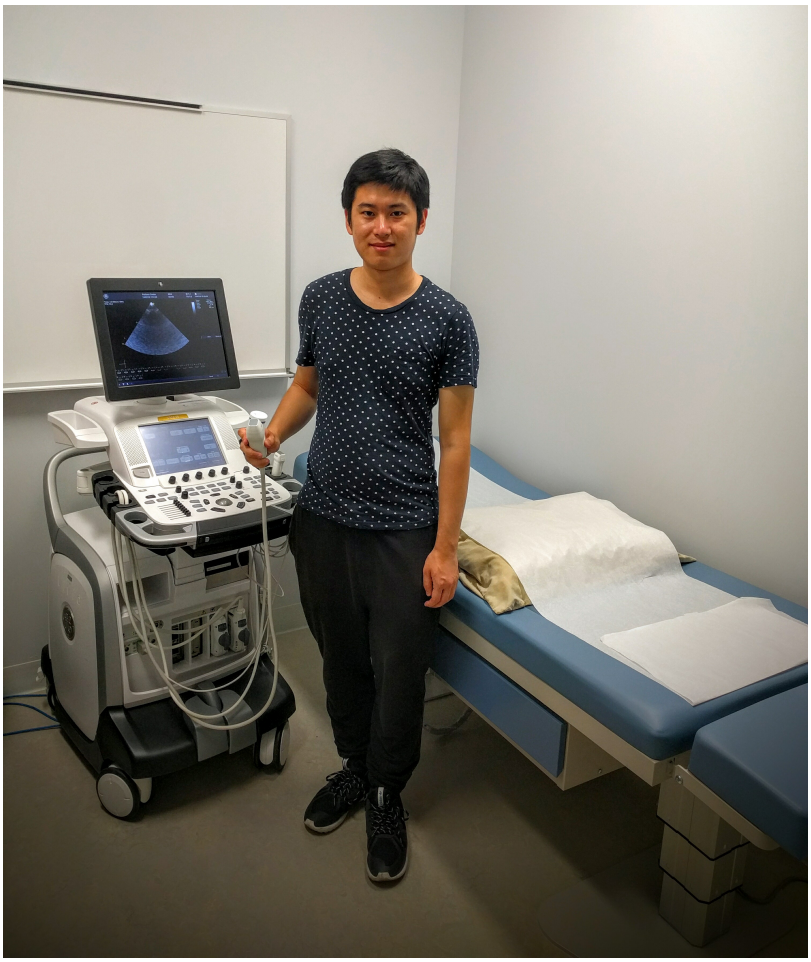

Figure 1.2: A GE Vivid E9 US machine.

There are various types of probes developed for different imaging purposes, among which three major types are: linear probe, curvilinear probe and phased array probe. The shapes of these three types are shown in Fig. 1.3. The linear probe transmits and receives high frequency US waves in order to collect high-quality US images near the patient surface, and

is ideal for vascular applications and breast imaging. Whereas the curvilinear probe operates at lower frequencies to reduce the attenuation and therefore make US waves go further into the body. Normally it is used for abdominal applications and diagnosis of organs. The biggest advantage of the phased array probe is that it gives a wide field of view over deep structures within a small footprint, which makes it appropriate for cardiac application and chest imaging as the US waves are beamed between ribs. The images in our neurosurgery work were also acquired using the phased array probe because of its convenience in acquisition.

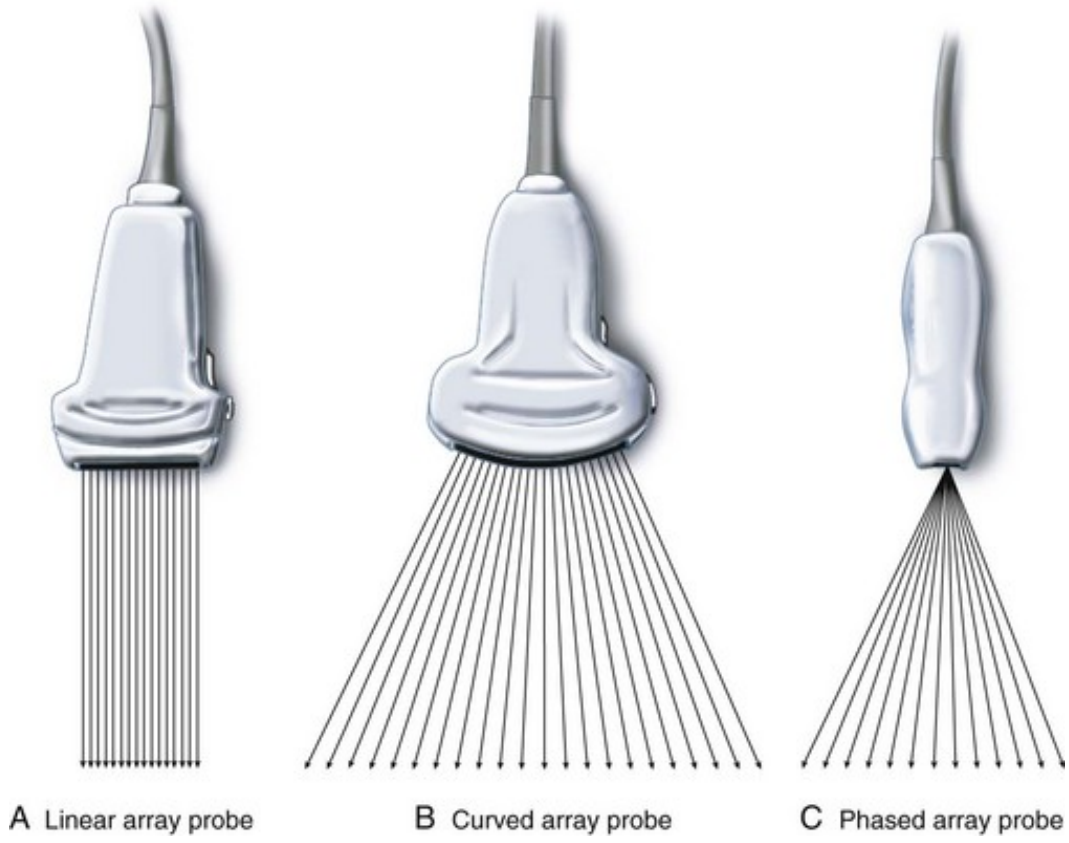

Figure 1.3: US probes.

Image courtesy of: http://oftankonyv.reak.bme.hu

Another classification of US imaging can be made based on image types. Traditional US images are 2D, which means US waves are transmitted and received in a single plane. More advanced technology has led to the application of 3D US scans. These 3D volumes are integrated by a sophisticated computer software from 2D images of different collection angles. Generally 3D US scans provide a better demonstration of the objective tissue, and are particularly useful in detection of malignant tumors, visualization of vessels and observation of development of the fetus.

An additional expansion of US imaging is Doppler US, which is based on the Doppler effect. The frequency of received echoes will be changed if the object reflecting US waves moves. When the object approaches the transducer, the frequency increases accordingly, whereas when the object is moving away from the transducer, the frequency decreases. Based on the Doppler effect we can compute the speed of the object from the changes of frequency, and therefore, Doppler US is particularly ideal for the measurement of the rate of blood inside vessels.

US imaging becomes very popular these days in diagnosis and treatment. Compared with magnetic resonance imaging (MRI), which is extremely expensive and requires dedicated operation rooms, US imaging is convenient and significantly less expensive. Besides, US imaging provides high quality images for soft tissue structures, making it an ideal imaging tool for soft tissues such as prostate, abdomen and breast [2]. Moreover, it is non-invasive and with quick acquisition speed, therefore it can be utilized in real-time monitoring in radiotherapy.

However, US imaging also suffers from some inherent drawbacks. Normally US volumes involve image artifacts, which makes them very difficult to analyze. Besides, the intensity of the same tissue can vary in two US scans due to changes of the insonification angle and shadows. Therefore, US images can not be used directly in radiotherapy process, and an US imaging framework is significantly important to help the surgeon analyze the data.

1.2 Image registration

Image registration refers to transformation of different images into one coordinate system. It has been widely used in many areas including medical imaging, object recognition and analyzing remote sensing data. We mainly talk about the medical application of image registration in this thesis. Generally, two or more images are registered when we perform registration, depending on the purpose of the registration technique. According to the correspondence, registration can be classified into intensity-based and feature-based methods. Intensity-based methods utilize intensity patterns for alignment, whereas feature-based algorithms use corresponding features such as points and lines to align images.

Another classification can be made based on the deformation models used in registration. One type is called rigid registration, which includes rotation, translation and reflection. Rigid registration is very simple, convenient and fast to perform, however it is only accurate in some applications such as bone imaging and provides relatively few parameters for deformation. The demand of dedicated longitudinal and cross-sectional brain studies has led

to the development of more complicated methods which have the ability to align images locally, called deformable registration. In [3], two deformable registration methods inspired by Demons [4] and Free-Form Deformations using B-splines [5] are demonstrated, and the bright future and inherent challenges of deformable registration are discussed. In [6], a recent review of image registration over past two decades is provided, and two related issues (validation of registration and the clinical usage of registration methods) are shown to be ongoing focus, leading to the conclusion that image registration has evolved but still needs further research.

In classical registration frameworks, one image is denoted as the fixed image, which means it does not move in the process of registration. The other image is referred to as the moving image, which is deformed through the process of registration to be aligned with the fixed image. However, several issues arise in such registration framework: the resulting transformation is not symmetric with respect to the two images, and therefore is biased on the selection of the moving image domain. Also, the deformation is not necessarily invertible, and can cause physically implausible folds or ruptures. To overcome these problems, inverse-consistent registration methods have been proposed in [7, 8]. They reduce bias by calculating forward and backward transformations $\mathbf{T_1}$ and $\mathbf{T_2}$, and penalize the difference between $\mathbf{T_1} \circ \mathbf{T_2}$ and the identity transformation. Another solution is to use symmetric algorithms [9], which are different with inverse-consistent methods but with the same intention. Instead of penalizing the difference, these algorithms solve the asymmetry following two manners. One selection is to construct a symmetric cost function in registration process. The other choice

is to calculate forward and backward transformation fields simultaneously when optimize the cost function. These two deformation fields map the two images into a middle image. The final deformation field from one image to another is calculated by inverting one field and composing it with the other deformation field.

One important factor in image registration is the selection of similarity metric. There are numerous measurements for similarity, depending on different conditions. Mutual information (MI) [10,11] measures the dependence of images, rendering it a very efficient and popular similarity metric in registration, especially in multi-modality registration. Specifically, it calculates the statistical relationship of two images based on intensity values, and maximizes the joint information of these two images to align them. However, as a global measurement it requires large window sizes and therefore is inaccurate for local estimation. In addition, since we need to calculate the shared information of two images in mutual information, the computation is inefficient and time-consuming.

Sum of squared difference (SSD) measures the average difference of intensity values at corresponding pixels in two images, and turns out to be another efficient similarity metric in registration. It is one of the simplest measures of images since it calculates the squared difference of intensity values at corresponding pixels and add the difference together to construct a global measurement. With its simplicity, which is its biggest advantage, SSD appears to be computationally efficient and easy to be optimized. However, it lacks the ability to adapt to affine intensity variations in images.

Normalized cross correlation (NCC) is aiming to deal with the situation in which the intensity of images varies due to different acquisition angles or parameters. With this metric, the intensity of pixels is normalized first, which is done by subtracting the mean and dividing by the standard deviation. And then the cross correlation of the normalized images will be calculated. The largest advantage of NCC over other metrics is that it is insensitive to affine intensity variations in images, making it an ideal similarity metric for US images. Besides, NCC is in the range of -1 to 1, which makes it suitable for numerical computations.

1.3 Neurosurgery

Neurosurgery is the surgery that treats the disorder of the nervous system using surgical approaches. It includes prevention, diagnosis, treatment, and rehabilitation. In this thesis, we only talk about diagnosis and treatment. Fig. 1.4 shows an example of neurosurgery images, which is a tumor in the brain.

Cancer is one of the major diseases that threaten human health, and is expected to outpace heart diseases as the largest factor in the future [12]. Cancer is caused by cancerous tumors, which proliferate abnormally, and proliferating cells may transfer to and invade other parts of the body. The other type is benign tumors, which are unable to spread to other areas of the body and provide no threat to adjacent tissue. Cancer appears in almost everywhere in the human body, and brings different threats to the patient. Among all types of cancer, brain cancer is most harmful to human health since brain tumors are difficult to be removed and

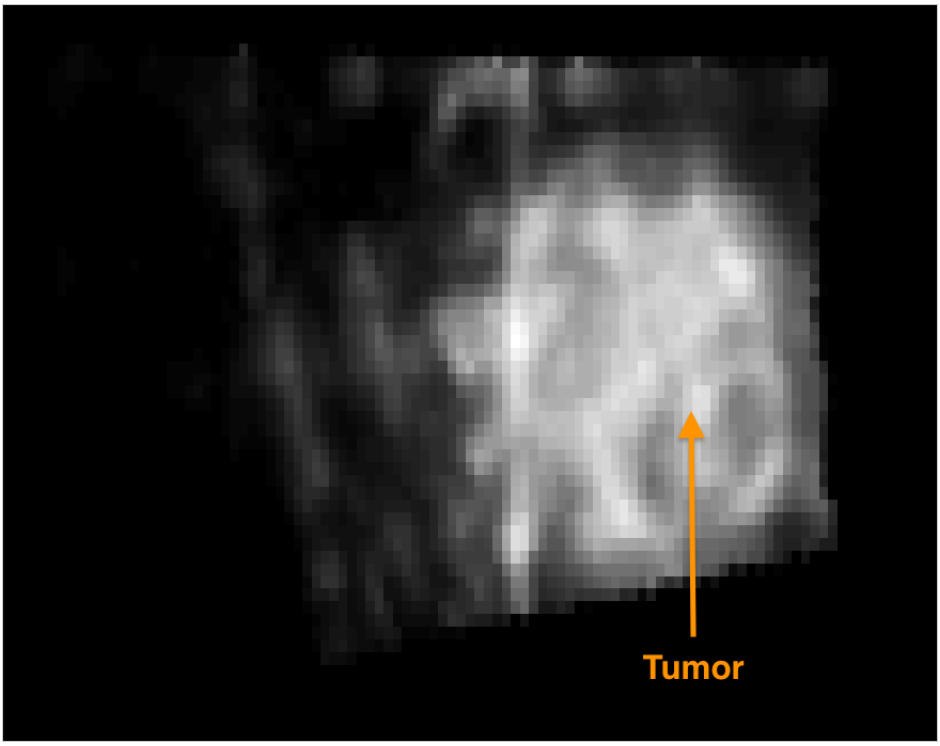

Figure 1.4: US image collected during neurosurgery. The orange arrow points to a brain tumor.

their invasion to the brain will cause cognitive deficit to the patient. Therefore, the most important part in neurosurgery is the diagnosis and treatment of brain tumors, which is normally achieved with the help of computed tomography (CT), MR or US images. These methods all have advantages and disadvantages, and are used for different purposes.

When there are symptoms like headaches or cognitive disorder in patients, the physician will give a diagnosis regarding tumors to the patient based on a CT or MR scan, since these imaging methods provide high quality images for tissue. These images provide background essential to help guide potential further testing, treatment options and timelines for possible surgery. In the treatment (surgery) stage, in order to remove necessary tumors while avoiding

causing side effects to the patient, neuro-navigation systems are usually used in many medical sites where image-to-patient registration is performed by selecting corresponding landmarks in the pre-operative MR image and on the skin. Unfortunately, several factors such as tissue shift and inherent landmark deviations render this registration inaccurate. To achieve the visualization of the brain during surgery, intra-operative MR has been popularly utilized. However, with the high demand of expenses and operation rooms, intra-operative MR is only feasible in large medical institutions, which significantly hinders its wide application in neurosurgery. The disadvantages of these imaging methods have led to the use of intra-operative US imaging, which is with low cost and fast acquisition time.

1.4 Prostate radiotherapy

Prostate cancer has become the third most common cancer in the world and shows a significant increase in the incidence and mortality especially in England and Wales [13]. Radiotherapy, referring to the technology destroying tumor cells using ionizing radiation while avoiding radiation exposure to healthy tissue, has been shown to be an effective treatment and the standard care in locally advanced or unresectable prostate cancer [14].

Prostate motion can be categorized into two types: intrafraction (during the fraction of treatment) and interfraction (between the fractions of treatment) [15]. Intrafraction motion is mainly contributed by respiratory and cardiac motion while interfraction motion is caused by daily changes in patient position and condition, such as weight gain/loss. This motion

significantly renders the initial position of the prostate inaccurate. Large margins must be placed around the prostate if no correction would be done, which runs counter to the intension of accurately targeting the tumor and reducing the side effects. Conventional solutions to interfraction motion include megavoltage X-ray portal imaging, kilovoltage X-ray imaging or cone-beam CT (CBCT) of bony anatomy and adjusting the patient's position according to the comparison of pre-treatment (simulation) and treatment images. However this correction may be inaccurate since the prostate can move freely with respect to bony anatomy, which renders radiotherapy based on these correction still need large margins. Fiducial markers (FMs) are also utilized to aid interfraction motion correction. However the implantation of markers, whilst straightforward, requires an additional procedure and the administration of prophylactic antibiotics [16].

The advance of imaging techniques has led to the development of image-guided radiotherapy. Initially, a simulation image is collected in the planning stage. A reference position volume (RPV) is defined by drawing a 3D contour of the prostate based on the simulation image. In the treatment stage, treatment images are collected before each fraction. These images are compared to the simulation image to calculate the couch shift necessary to correct for interfration motion. One great challenge in this process is the reposition of the prostate region, since tissue deforms significantly after the collection of the simulation image. Therefore the reposition of the prostate region in treatment images is significantly important and has attracted serious concerns in radiotherapy.

Chapter 2

Registration of Ultrasound Volumes with Non-corresponding Regions in Neurosurgery

2.1 Introduction

The problem of residual tumor has attracted serious concern in tumor surgery. The infiltrating nature of brain tumors and the possibility of causing cognitive deficit to the patient after the resection of critical parts lead to residual tumor in as much as 64% of patients [17]. Therefore, neuro-navigation systems are commonly used in many sites where image-to-patient registration is performed by selecting corresponding landmarks in the pre-operative MR image

and on the skin. Unfortunately, this registration is inaccurate for two main reasons. First, brain tissue deforms during surgery and after craniotomy as much as 50 mm [18], which renders pre-operative MR images inaccurate. Second, the selection of corresponding landmarks on the skin and in the MR image is inaccurate, and leads to large registration errors. To allow the visualization of the brain during surgery, intra-operative MR has been used. However, intra-operative MR is extremely expensive and requires dedicated operation rooms as well as MR compatible equipment, which hinder its wide application in surgical operations.

Alternatively, intra-operative US imaging is convenient and significantly less expensive, and as such, is used in many neurological centers. An US volume is obtained before tumor resection to allow the visualization of tumor boundaries and critical brain structures. More US scans are acquired during and after resection to help the surgeon locate and minimize residual tumor. Unsgård *et al.* [19] and Solheim *et al.* [20] demonstrated the significance of intra-operative US imaging in neurosurgery based on more than 900 operations. El Beltagy *et al.* [21] collected pre-, during and post-resection US images, as well as MR images before and immediately (within 48 h) after surgery, and concluded that intra-operative US was useful in identifying tumor boundaries and minimizing residual tumor. Recently, Renovanz *et al.* [22], Petridis *et al.* [23], Coburger *et al.* [24] and Moiyadi & Shetty [25] performed a retrospective analysis of the Gross-Total Resection (GTR) of patients who underwent US guided neurosurgery and concluded that US could be effective in achieving GTR, especially for low-grade glioma.

It is generally more difficult for neurosurgeons to interpret post-operative US images due to resection of tissue and large brain shift. In addition, the large difference in acoustic impedance between the saline water solution, as well as the blood clotting agent that is placed around resection cavities create strong reflection at the boundary of resection. This strong reflection can overshadow possible residual tumor in post-resection US images. In Selbekk *et al.* [26], different underlying reasons of image artifacts and their impact on the quality of US images were demonstrated, and a novel acoustic coupling fluid method was proposed to reduce these artifacts.

Registration of pre- and post-operation US volumes is of significant clinical interest: it simplifies interpretation of post-resection images, and may help in identifying residual tumor. This registration is challenging for several reasons. First, both the deformation and imaging data are in 3D, entailing computationally demanding 3D calculations. Second, shadowing and enhancing, which are well-known artifacts in US imaging [27], are common in post-resection images. Therefore, the intensity of the same tissue can be very different in pre- and post-resection US volumes. Finally, because of the removal of partial tissue during resection, some regions of pre- and post-resection images do not correspond to each other.

Registration of US volumes is an active field of research with numerous new advances. US registration methods can be categorized into feature-based [28–30] and intensity-based [31–35]. Feature-based methods first find corresponding points in the two US volumes, and

then use these correspondences to find the registration transformation. Intensity-based methods rely on similarity metrics such as NCC [32, 33, 35], mutual information [34], or phase differences [31]. Another categorization can be made based on the transformation, which can be rigid [29, 31, 32, 34, 35] or deformable [28, 30, 33]. Deformable registration usually has significantly more degrees of freedom, and is therefore more challenging.

The detection of non-corresponding regions is another area of related work. Banerjee *et al.* [36] performed affine registration between two volumes to compensate for the motion of liver, while outliers were detected and rejected with a novel outlier rejection algorithm based on a geometric consistency term. Gao *et al.* [37] developed a probabilistic and outlier-adaptive algorithm using an Expectation Maximization (EM) framework wherein the ratio of outlier data was updated in every iteration. Khamene *et al.* [38] first obtained a prior intensity distribution of non-corresponding regions in the training step. In the registration step, the transformations that mapped the intensity distribution of outlier regions to the prior distribution were favored.

A closely related work registered pre- and post-resection US images of neurosurgery by first performing manual segmentation of resection cavities [33]. Another related technique called RESOUND [1] was based on gradient descent optimization of a regularized cost function with deformable free-form B-splines transformation. An important issue with RESOUND, however, is that free-form B-splines are not invertible and can generate folds and ruptures that are physically unrealistic. Another issue lies in the optimization scheme used in

RESOUND, which is based on gradient descent and therefore has a linear convergence rate. This can hinder the clinical application of RESOUND where robust and accurate performance is critical.

In this chapter, we build on RESOUND and propose a novel robust deformable registration technique for the alignment of pre- and post-resection US images called Nonrigid Symmetric Registration (NSR) [39]. Two main contributions of this work are as follows: 1) We incorporate symmetric deformation fields that are invertible and an Efficient Second-order Minimization (ESM) method [40] into our registration technique to create high quality deformation fields while maintaining a fast and reliable convergence. To the best of our knowledge, this is the first time symmetric deformation and ESM are used in US registration. 2) We propose an accurate outlier detection approach and validate its effectiveness on both simulated images and clinical data. We evaluate our framework on US images of 13 patients quantitatively and qualitatively, and demonstrate that NSR detects non-corresponding regions and registers these challenging images accurately and efficiently. A shorter version of this chapter was recently published in [41].

2.2 Methods

2.2.1 Deformable registration

Numerous registration algorithms, including RESOUND, find a deformable transformation that maps one image to another. Several issues arise in such registration framework: the resulting transformation is not symmetric with respect to the two images, and therefore is biased on the selection of the moving image domain. Also, the deformation is not necessarily invertible, and can cause physically implausible folds or ruptures. To overcome these problems, inverse-consistent registration methods have been proposed in [7, 8]. They reduce bias by calculating forward and backward transformations $\mathbf{T_1}$ and $\mathbf{T_2}$, and penalize the difference between $\mathbf{T_1} \circ \mathbf{T_2}$ and the identity transformation. In this work, we utilize a symmetric and inverse-consistent method similar to [42], and apply the iterative approach of [43] to invert transformations. Full forward and backward deformation can then be calculated as $\mathbf{T_1}(0.5) \circ \mathbf{T_2}(0.5)^{-1}$ and $\mathbf{T_2}(0.5) \circ \mathbf{T_1}(0.5)^{-1}$ respectively, where 0.5 means half of the deformation field and $\circ$ represents composition of transformations.

The outline of our registration framework is shown in Fig. 2.1. Let $\mathbf{V_1}$ and $\mathbf{V_2}$ represent two US volumes, and $\mathbf{x} \subset R_d$ denote global coordinates, where $d = 3$ for 3D volumetric images. Also, $\mathbf{T_u}(\mathbf{x}) = \mathbf{x} + \mathbf{u}$ represents forward and backward deformations. The goal of our registration framework is to find the 3D deformation fields $\mathbf{u_1}$ from $\mathbf{V_1}$ to $\mathbf{V_2}$ and $\mathbf{u_2}$ from $\mathbf{V_2}$ to $\mathbf{V_1}$. To find $\mathbf{u_1}$ and $\mathbf{u_2}$, a regularized cost function can be formulated as:

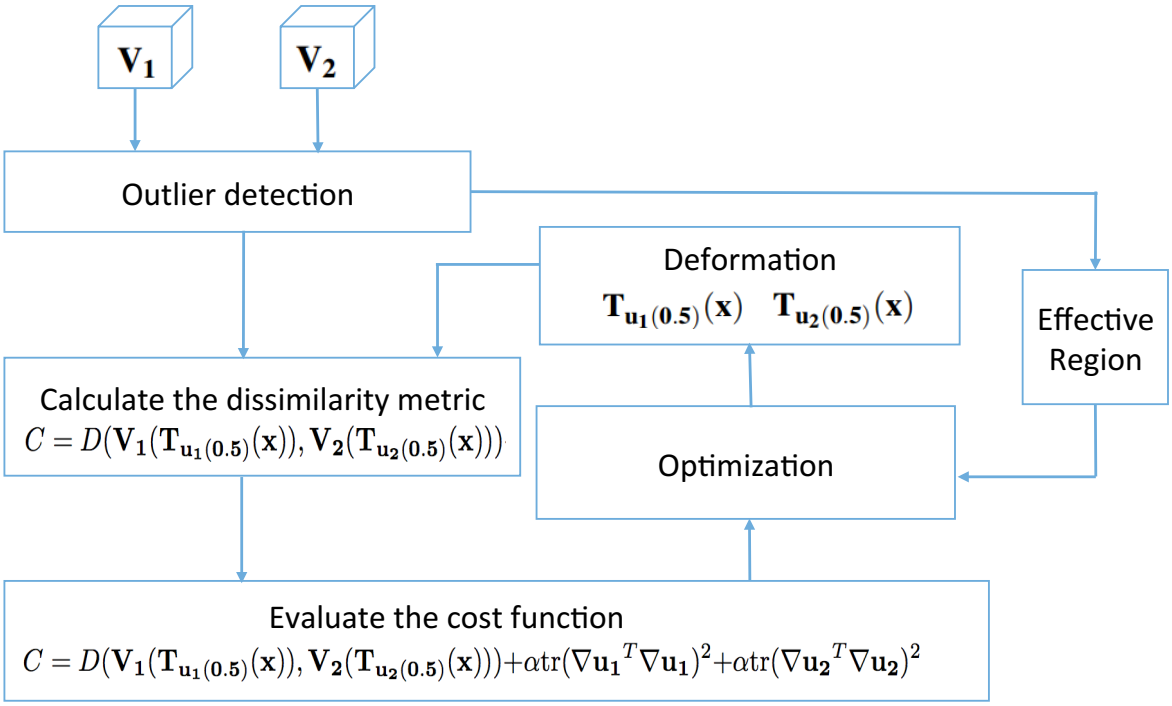

Figure 2.1: Outline of the NSR registration technique.

$$C = D(\mathbf{V_1}(\mathbf{T_{u_1(0.5)}}(\mathbf{x})), \mathbf{V_2}(\mathbf{T_{u_2(0.5)}}(\mathbf{x}))) + \alpha \mathrm{tr}(\nabla \mathbf{u_1}^T \nabla \mathbf{u_1})^2 + \alpha \mathrm{tr}(\nabla \mathbf{u_2}^T \nabla \mathbf{u_2})^2 \quad (2.1)$$

where D is a dissimilarity metric, $\mathbf{V_1}(\mathbf{T_{u_1(0.5)}}(\mathbf{x}))$ is the middle volume from $\mathbf{V_1}$, $\mathbf{V_2}(\mathbf{T_{u_2(0.5)}}(\mathbf{x}))$ is the middle volume from $\mathbf{V_2}$, α is a regularization weight, tr is the trace operator and $\mathrm{tr}(\nabla \mathbf{u}^T \nabla \mathbf{u})^2$ is a diffusion regularization term.

The intensity of the same tissue can vary in two US scans due to changes of the insonification angle and shadowing and enhancing artifacts. We therefore select NCC as the

similarity metric, which is invariant to such intensity variations and further can be reliably computed over small patches. Instead of using $-\mathrm{NCC}$ as the dissimilarity metric, we use $-\mathrm{NCC}^2$ to employ quadratic optimization methods. Then we divide the volumes into small patches, calculating $-\mathrm{NCC}^2$ in each patch, and add the results up to generate a global cost:

$$D = -\frac{1}{N}\sum_{i=1}^{N}\rho_i^2 \tag{2.2}$$

$$\rho_i^2 = \frac{(\sum_{j=1}^{n}(V_{1j} - \overline{\mathbf{V_{1}}_i})(V_{2j} - \overline{\mathbf{V_{2}}_i}))^2}{\sum_{j=1}^{n}(V_{1j} - \overline{\mathbf{V_{1}}_i})^2 \sum_{j=1}^{n}(V_{2j} - \overline{\mathbf{V_{2}}_i})^2} \tag{2.3}$$

$$\mathbf{V_1} = \mathbf{V_1}(\mathbf{T}_{\mathbf{u_1}(0.5)}(\mathbf{x})), \mathbf{V_2} = \mathbf{V_2}(\mathbf{T}_{\mathbf{u_1}(0.5)}(\mathbf{x}))$$

where $\mathbf{V_{1}}_i$ and $\mathbf{V_{2}}_i$ are patch i in $\mathbf{V_1}$ and $\mathbf{V_2}$ respectively, V_{1j} and V_{2j} are the intensity of pixel j in patch i, $\overline{\mathbf{V_{1}}_i}$ and $\overline{\mathbf{V_{2}}_i}$ are the mean intensity of patch i, N is the number of patches in the volume and n is the number of pixels in each patch. The N patches are selected on a grid in image regions with high signal to noise ratios as elaborated in the next section.

2.2.2 Outlier detection

During neurosurgery, brain tumors are resected and therefore do not correspond to resection cavities in post-resection US images. Obviously, missing correspondences undermine the effectiveness of our work. Therefore we develop a novel outlier detection approach to

identify outliers and efficiently reduce the impact of non-correspondences between pre- and post-resection images.

In Rivaz *et al.* [44], directions of derivatives of NCC in individual pixels in each iteration was investigated to detect outliers. It was showed that the derivatives in non-corresponding regions pointed to random directions, while they generally pointed to the same direction in corresponding regions. These directions can be calculated using the vector $\frac{\partial \rho}{\partial \mathbf{u}}$ in each patch. Our new detection approach is based on this work, and further, we utilize an additional feature to improve the accuracy of detection. This feature is ρ, which is generally low for non-corresponding regions. Therefore, the metric r of a patch, which is used for outlier detection, is calculated using the following equations:

$$r_1 = \mathbf{std}(\frac{\partial \rho}{\partial \mathbf{u_1}}) - \beta \rho^2 \tag{2.4}$$

$$r_2 = \mathbf{std}(\frac{\partial \rho}{\partial \mathbf{u_2}}) - \beta \rho^2 \tag{2.5}$$

where β is a coefficient and $\mathbf{std}(\mathbf{v})$ is the standard deviation of the elements of vector $\mathbf{v}$. We will provide the analytic formula for $\frac{\partial \rho}{\partial \mathbf{u}}$ in Section 2.3. This metric will be assigned to each pixel of that patch. If there are overlaps among patches, we will divide the sum of metrics in a pixel by the overlapping times. After doing this for all patches, a 3D volume whose size is the same as that of the US volume is constructed. We call this 3D volume "Initial Pattern". After setting a threshold for the "Initial Pattern", we treat elements whose value is greater than the

threshold as outliers, and accordingly obtain a 3D binary volume showing corresponding (1) and non-corresponding (0) regions. This volume is composed of the information of outliers, which will be useful in the registration process. In addition to this mask, we construct a second volume wherein pixels with intensity less than 3% of the maximum intensity (i.e. with very low signal to noise ratio (SNR)) are assigned a value of 0. An "Effective Region" is obtained by combining these two volumes, where 0 pixels represent either outliers or regions suffering from low SNR. During registration, the dissimilarity metric will not be computed in regions of the "Effective Region" with zero values.

In order to validate the effectiveness of our outlier detection algorithm, we simulate our method on two images, which are shown in Fig. 2.2 (a) and (b). In this test, we only verify our outlier detection algorithm, without the registration process. The contents of these two images are identical, being displaced by five pixels in the vertical direction. The circular region in (b) represents an outlier region. After performing our outlier detection algorithm, we obtain the "Initial Pattern" in (c) and (d), wherein we can clearly and accurately distinguish outliers (non-corresponding regions) from inliers (corresponding regions). In Fig. 2.3, Quiver inlier and Quiver outlier demonstrate the Jacobian of NCC calculated at each pixel in an inlier patch and an outlier patch respectively. The location of the inlier patch and outlier patch is marked by red and magenta boxes in Fig. 2.2 (d) respectively. As can be seen from these two images, pixels in the outlier patch generally move in random directions, whereas pixels in inlier regions move consistently. We repeated this experiment on 10 different pairs of US images and outlier

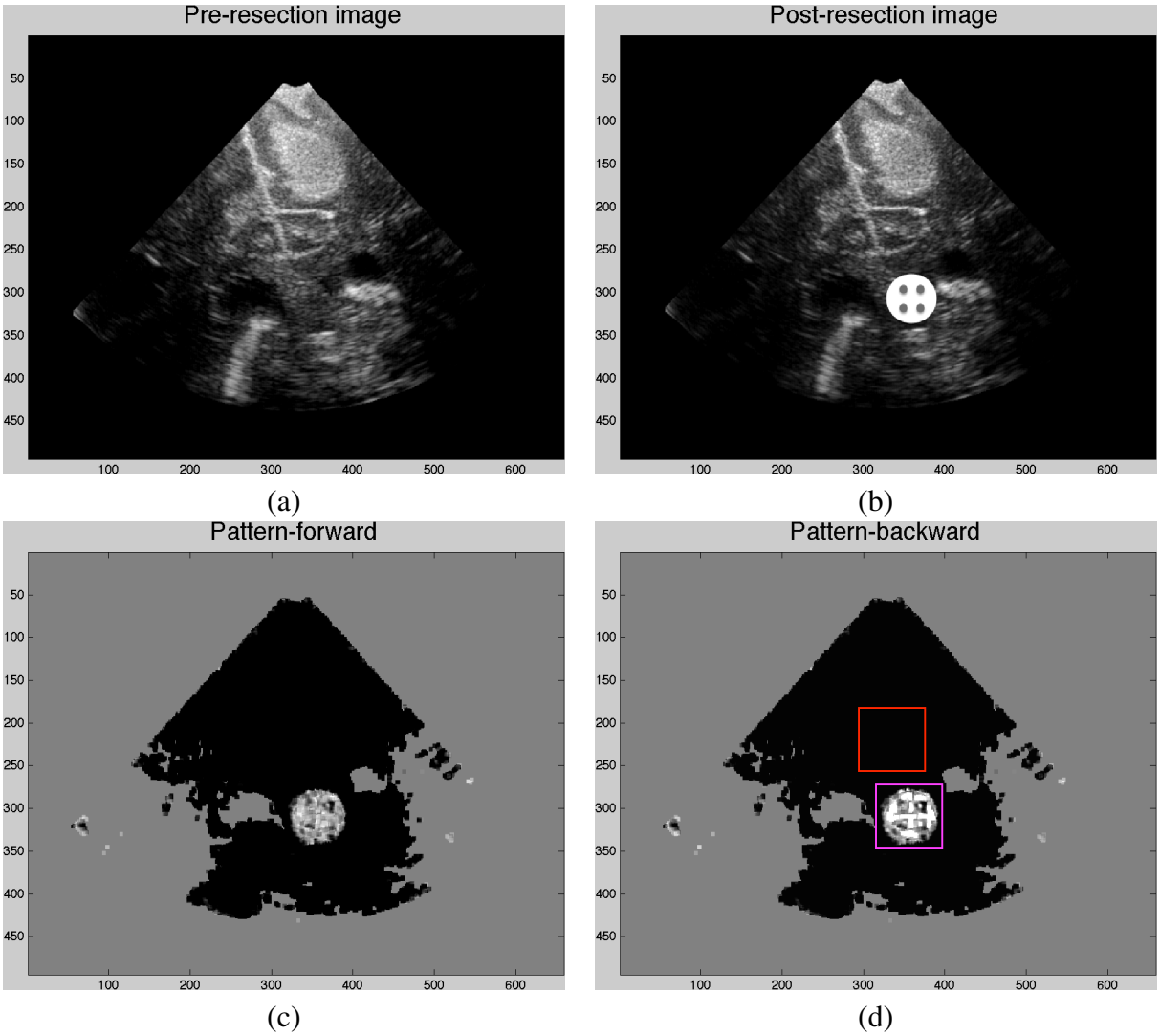

Figure 2.2: Demonstration of the outlier detection technique. (a) is an image from the BITE database, while the contents in (b) are identical but displaced by 5 pixels in the vertical direction. The circular region in (b) represents an outlier region, simulating tissue resection. In pattern images (c) and (d), the black parts represent the regions with low metric, corresponding to inlier regions, whereas the bright parts indicate outlier regions. An inlier and an outlier patch are shown in (d) in red and magenta respectively.

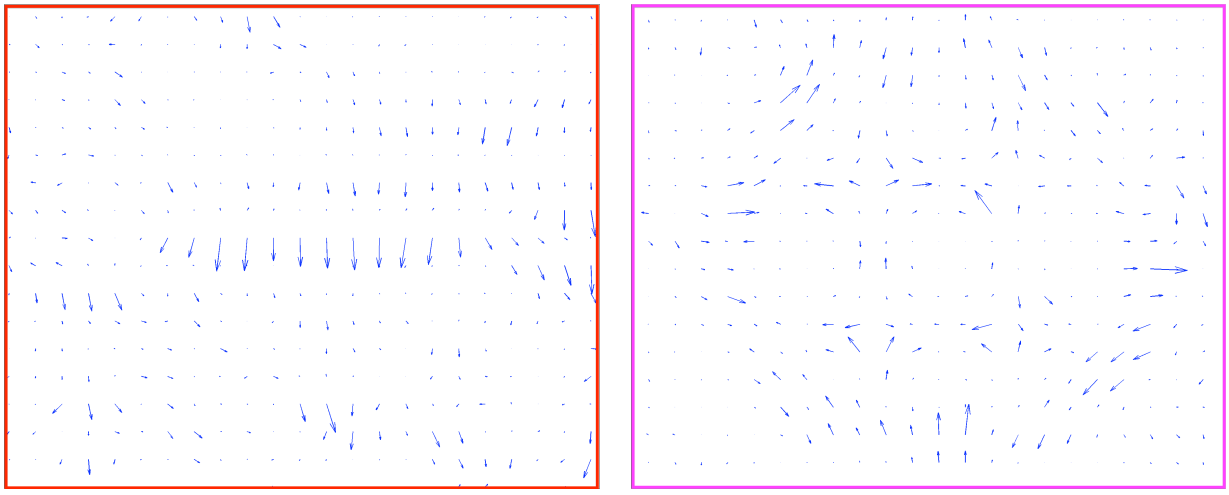

Quiver inlier Quiver outlier

Figure 2.3: Quiver inlier and Quiver outlier show the Jacobian of NCC at each pixel in the inlier and outlier patches respectively.

patterns, and obtained similar results.

2.3 Optimization

To calculate the optimal deformation fields, we have to minimize the cost function. Usually, non-linear minimization problems are solved in an iterative manner. Several optimization algorithms can be applied to obtain incremental updates. Steepest gradient descent (SGD) is used in [1] to optimize the cost function. However, SGD always moves perpendicularly to isolines and generally has a low convergence rate [40]. The Gauss-Newton method can archive a quadratic convergence rate, but the cost function must be of a specific form. The Levenberg-Marquardt minimization method is indeed efficient for optimization. However since it is a mixture of the Gauss-Newton method and SGD, it has a convergence rate between linear and

quadratic.

In this work, we use pseudo-inverse of the mean of Jacobian matrices as the optimization method, which is one of the ESM methods proposed in [40]. ESM uses first-order derivatives to approximate second-order derivatives, making optimization computationally efficient. In this algorithm, forward deformation Jacobian is combined with backward one to generate more accurate incremental updates. Despite the fact that ESM uses only first-order derivatives, it is shown to have a cubic convergence rate [45]. When we calculate $-\mathrm{NCC}^2$ in a patch, we can also obtain the value of NCC and the derivatives of NCC with respect to the intensity of each pixel in that patch. We assign the NCC to each pixel in that patch to act as the residual function:

$$\frac{\partial \rho_i}{\partial \mathbf{I}} = \frac{1}{|\mathbf{V_a}||\mathbf{V_b}|}(\mathbf{V_a} - \frac{\langle \mathbf{V_a}, \mathbf{V_b} \rangle}{|\mathbf{V_b}|^2}\mathbf{V_b}) \tag{2.6}$$

$$\mathbf{V_a} = \mathbf{V_{1}}_i - \overline{\mathbf{V_{1}}_i}, \mathbf{V_b} = \mathbf{V_{2}}_i - \overline{\mathbf{V_{1}}_i}$$

where ρ_i is the NCC of patch i and $\frac{\partial \rho_i}{\partial \mathbf{I}}$ is the derivative vector of NCC with respect to the intensity of each pixel in patch i. Since we need the NCC value and its derivative at each voxel, we define $\mathbf{P}$ as:

$$\mathbf{P} = \begin{bmatrix} \rho_1 & \rho_2 & \cdots & \rho_j & \cdots & \rho_M \end{bmatrix}^T \tag{2.7}$$

where ρ_j is the NCC value computed at pixel j and M is the total number of voxels in the

volume. In an abuse of notation, we define $\frac{\partial \mathbf{P}}{\partial \mathbf{I}}$ as:

$$\frac{\partial \mathbf{P}}{\partial \mathbf{I}} = \begin{bmatrix} \frac{\partial \rho_1}{\partial I_1} & \frac{\partial \rho_2}{\partial I_2} & \cdots & \frac{\partial \rho_j}{\partial I_j} & \cdots & \frac{\partial \rho_M}{\partial I_M} \end{bmatrix}^T \tag{2.8}$$

where $\frac{\partial \rho_j}{\partial I_j}$ is the derivative of NCC in pixel j with respect to the intensity of that pixel. Note that some patches may have overlapping voxels. Using the chain rule, we obtain:

$$\nabla_{\mathbf{u_1}} \mathbf{P} = \frac{\partial \mathbf{P}}{\partial \mathbf{u_1}} = \frac{\partial \mathbf{I_{V_1}}}{\partial \mathbf{u_1}} \frac{\partial \mathbf{P}}{\partial \mathbf{I_{V_1}}} \tag{2.9}$$

$$\nabla_{\mathbf{u_2}} \mathbf{P} = \frac{\partial \mathbf{P}}{\partial \mathbf{u_2}} = \frac{\partial \mathbf{I_{V_2}}}{\partial \mathbf{u_2}} \frac{\partial \mathbf{P}}{\partial \mathbf{I_{V_2}}} \tag{2.10}$$

where $\frac{\partial \mathbf{I_V}}{\partial \mathbf{u}}$ is the gradient of intensity and $\nabla_{\mathbf{u_1}}$ and $\nabla_{\mathbf{u_2}}$ are the Jacobians with respect to forward and backward deformation fields respectively. Given the Jacobians of two directions, we can find the optimal deformation fields following an iterative rule. First the forward Jacobian is combined with the backward Jacobian to generate two average Jacobians, which will be used in the subsequent computation:

$$\nabla_{\mathbf{u_1}} \mathbf{P_{av}} = \frac{1}{2}(\nabla_{\mathbf{u_1}} \mathbf{P} - \nabla_{\mathbf{u_2}} \mathbf{P}) \tag{2.11}$$

$$\nabla_{\mathbf{u_2}} \mathbf{P_{av}} = \frac{1}{2}(\nabla_{\mathbf{u_2}} \mathbf{P} - \nabla_{\mathbf{u_1}} \mathbf{P}) \tag{2.12}$$

where $\nabla_{\mathbf{u_1}}\mathbf{P_{av}}$ and $\nabla_{\mathbf{u_2}}\mathbf{P_{av}}$ are average Jacobians for forward and backward deformations respectively. These two terms are denoted by $\nabla_{\mathbf{u_1}}\mathbf{P}$ and $\nabla_{\mathbf{u_2}}\mathbf{P}$ hereafter to prevent notation clutter. Incremental updates can then be computed with the rule $(\nabla_{\mathbf{u}}\mathbf{P}^T\nabla_{\mathbf{u}}\mathbf{P})\mathbf{\Delta_u} = \nabla_{\mathbf{u}}\mathbf{P}^T\mathbf{P}$, where $\mathbf{P}$ is the vector of NCC (shown in Eq. 2.7) that acts as the residual function. Because of the diffusion regularization term, the update rule becomes [42]:

$$(\nabla_{\mathbf{u}}\mathbf{P}^T\nabla_{\mathbf{u}}\mathbf{P} + \alpha\mathbf{I})\mathbf{\Delta_u} = \nabla_{\mathbf{u}}\mathbf{P}^T\mathbf{P} + \alpha\nabla^{\mathbf{2}}\mathbf{u_{previous}} \tag{2.13}$$

where $\mathbf{I}$ is an identity matrix, α is a coefficient and $\nabla^{\mathbf{2}}\mathbf{u_{previous}}$ is Laplacian of the sum of all previous updates. The incremental update $\mathbf{\Delta_u}$ is calculated using a successive over-relaxation solver. Compared with the Jacobi and Gauss-Seidel methods, it is more accurate and flexible for solving equations. Subsequently, deformation fields can be updated by adding the incremental updates:

$$\mathbf{u_1}^{t+1} = \mathbf{u_1}^{t} + \lambda\mathbf{\Delta_{u_1}} \tag{2.14}$$

$$\mathbf{u_2}^{t+1} = \mathbf{u_2}^{t} + \lambda\mathbf{\Delta_{u_2}} \tag{2.15}$$

where λ is a step size and $\mathbf{\Delta_{u_1}}$ and $\mathbf{\Delta_{u_2}}$ are incremental updates for forward and backward deformation fields respectively. Since we use the NCC vector as the residual function, whose elements approach one at the optimal alignment, we utilize a progressively smaller step size strategy. In each iteration, because of the symmetric and inverse-consistent registration, full

deformation fields are calculated by:

$$\mathbf{u_{1\,full}} = \mathbf{u_1}(0.5) \circ \mathbf{u_2}(0.5)^{-1} \tag{2.16}$$

$$\mathbf{u_{2\,full}} = \mathbf{u_1}(0.5)^{-1} \circ \mathbf{u_2}(0.5) \tag{2.17}$$

Moreover, multi-level hierarchical registration from coarse to fine levels is applied in this work to speed up the registration process and avoid getting trapped in local minima.

2.4 Experiments and results

To validate the performance of our outlier detection algorithm and our registration framework, pre- and post-resection US images of 13 patients are utilized from the BITE database [46]. The experimental procedures involving human subjects in BITE were approved by McGill University's Institutional Review Board. NSR takes approximately 40 seconds on a 3GHz processor to perform a typical 3D registration. These volumes are reconstructed from 2D US image sequences with the voxel size of $1\ mm \times 1\ mm \times 1\ mm$. And these datasets also include homologous anatomical landmarks in pre- and post-resection US volumes. The distribution of the landmarks of pre- and post-resection US volumes of one patient is shown in Fig. 2.4 as an example. To quantitatively measure the performance of NSR, we use the mean target registration errors (mTRE) metric, which shows the average distance between corresponding landmarks as follows. Let $\mathbf{x}$ and $\mathbf{x}'$ represent corresponding landmarks in $\mathbf{V_1}$

and $\mathbf{V_2}$ respectively, then mTRE can be calculated as [47]:

$$\mathrm{mTRE} = \frac{1}{l}\sum_{i}^{l}\|\mathbf{T_{u_1}}(\mathbf{x_i}) - \mathbf{x_i'}\| \tag{2.18}$$

where $\mathbf{T_{u_1}}$ is full forward deformation and l is the number of landmarks.

The original mTRE and final mTRE of all patients are shown in Table 2.1. As can be seen from the table, every mTRE decreases after NSR registration. Even the mTRE of patient 11, whose initial value of 10.5 mm decreases to 2.8 mm after NSR. We also perform t-tests between mTRE after NSR and initial mTRE, mTRE after RESOUND and initial mTRE respectively, and compare their *p*-values. The distributions of mTRE and minimum TRE of RESOUND and NSR in Fig. 2.5 show that NSR provides a more outstanding registration result. This improvement is obtained by both improved optimization and the symmetric and inverse-consistent approach.

There are two important limitations in BITE TRE values. First, in average, around 9 landmarks are selected in each 3D volume, and therefore, the landmarks only show registration accuracy in a very small portion of US volumes. Second, manually selected landmarks in BITE are only accurate up to 1.58 mm [33] and 1.4 mm [44]. Therefore, to further demonstrate the effectiveness of our registration framework and our outlier detection algorithm, pre- and post-registration alignments of images of four patients are shown in Figs. 2.6, 2.7, 2.8 and 2.9. The results in these four patients are representative of the performance of NSR in all patients, and are selected for two reasons. First, US images have distinctive contours that clearly

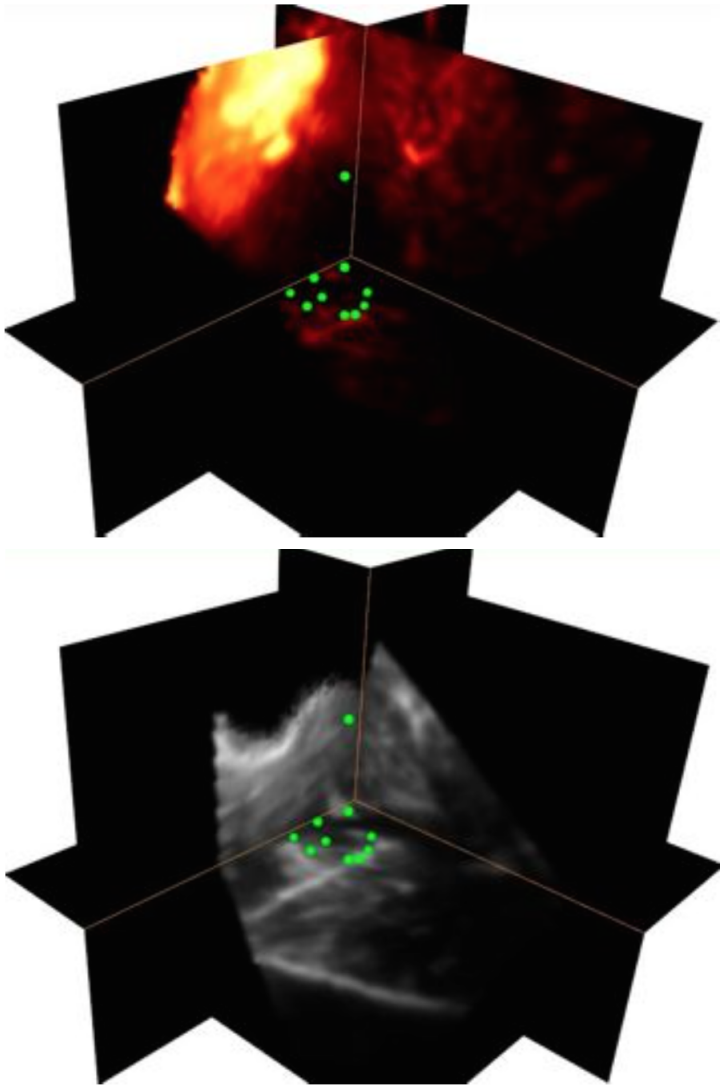

Figure 2.4: Ten corresponding landmarks in pre- (top) and post-resection (bottom) US volumes.

Table 2.1: mTRE values before and after registration with RESOUND and NSR. LGG and HGG represent low and high grade glioma respectively. The RESOUND data are from [1] and all smaller values are in bold. The *p*-values in the last row show the statistical significance of improvement over the initial mTRE.

Patient	Tumor type	Tumor size(cm^3)	Initial	RESOUND	NSR
P1	LGG	79.2	2.3(0.6-5.4)	1.8(0.5-4.0)	**1.4**(0.1-3.6)
P2	HGG	53.7	3.9(2.8-5.1)	1.4(0.5-1.9)	**1.2**(0.3-2.3)
P3	HGG	31.6	4.6(3.0-5.9)	1.4(0.7-2.2)	**1.2**(0.4-1.7)
P4	HGG	0.2	4.1(2.6-5.5)	1.2(0.3-2.4)	**1.1**(0.2-2.2)
P5	HGG	32.3	2.3(1.4-3.1)	**1.0**(0.2-1.7)	1.1(0.5-2.5)
P6	HGG	13.9	4.4(3.0-5.4)	**1.0**(0.4-1.7)	1.1(0.7-1.9)
P7	HGG	63.1	2.7(1.7-4.1)	1.7(0.9-3.6)	**1.4**(0.4-3.0)
P8	HGG	4.8	2.2(1.0-4.6)	1.4(0.6-3.2)	**1.3**(0.4-3.4)
P9	HGG	10.4	3.9(1.0-6.7)	**1.9**(0.7-4.1)	2.8(0.5-4.7)
P10	LGG	39.7	2.9(0.8-9.0)	2.2(0.6-5.3)	**2.2**(0.5-3.9)
P11	LGG	49.1	10.5(7.8-13.0)	**2.5**(1.1-4.2)	2.8(0.3-6.4)
P12	HGG	31.9	1.6(1.3-2.2)	**0.7**(0.2-1.6)	0.8(0.4-1.5)
P13	LGG	37.3	2.2(0.6-4.0)	**1.3**(0.2-2.8)	1.3(0.3-3.4)
mean	-	34.4	3.7(2.1-5.7)	**1.5**(0.5-3.0)	**1.5**(0.4-3.1)
p-value	-	-	-	0.0023	**0.0019**

show the alignment quality. Second, tumors are large enough to be visible in US images, and therefore the quality of alignment can be assessed in regions close to non-corresponding regions that are hard to register. For completeness, the results of the remaining nine patients are included in Appendix. A. To show the level of alignment between US images, we perform the following three steps: 1) Select an image from the pre-resection volume and the corresponding frame from the post-resection volume. 2) Automatically find edges of the pre-resection image using the Canny edge detection technique, and overlay the edges on the pre-resection frame in (a). 3) Overlay the edges of the pre-resection image on the post-resection frame in (b), which

shows the misalignment between pre- and post-resection volumes. In (c) and (d), the post-resection images after registration with RESOUND and NSR are shown respectively. While better alignment with the pre-resection image is clear in both (c) and (d), NSR substantially outperforms RESOUND. Improved alignments with NSR (over RESOUND) are pointed by magenta arrows in (d) and red arrows in (c) respectively. Such qualitative results have significant advantages over mTRE because they show the level of alignment over a much larger region, compared with few points used in mTRE (around 9/patient). Parts (e) and (f) show the "Effective Region" for both directions, where the regions inside the yellow contour are treated as inliners and all the other regions are deemed as outliers or low SNR regions. Parts (g) and (h) are overlay of the contour of "Effective Region" on the corresponding frame of the volume, and we use these pictures to demonstrate the effectiveness of our outlier detection algorithm. The results show that NSR can identify outliers and low SNR regions and register these challenging images accurately and efficiently.

2.5 Conclusion

A novel robust framework is proposed in this chapter for deformable registration of pre- and post-resection volumetric US images of neurosurgery. NCC, which is invariant to affine distortions of intensity values, is used as the similarity metric. ESM is used to optimize the regularized cost function to achieve fast and reliable registration. We use the symmetric and inverse-consistent approach to generate realistic deformation fields. Also, an outlier

detection method is proposed and utilized to identify and locate non-corresponding regions. NSR outperforms RESOUND, as indicated in our results, for two main reasons: the improved deformation model and more reliable optimization scheme.

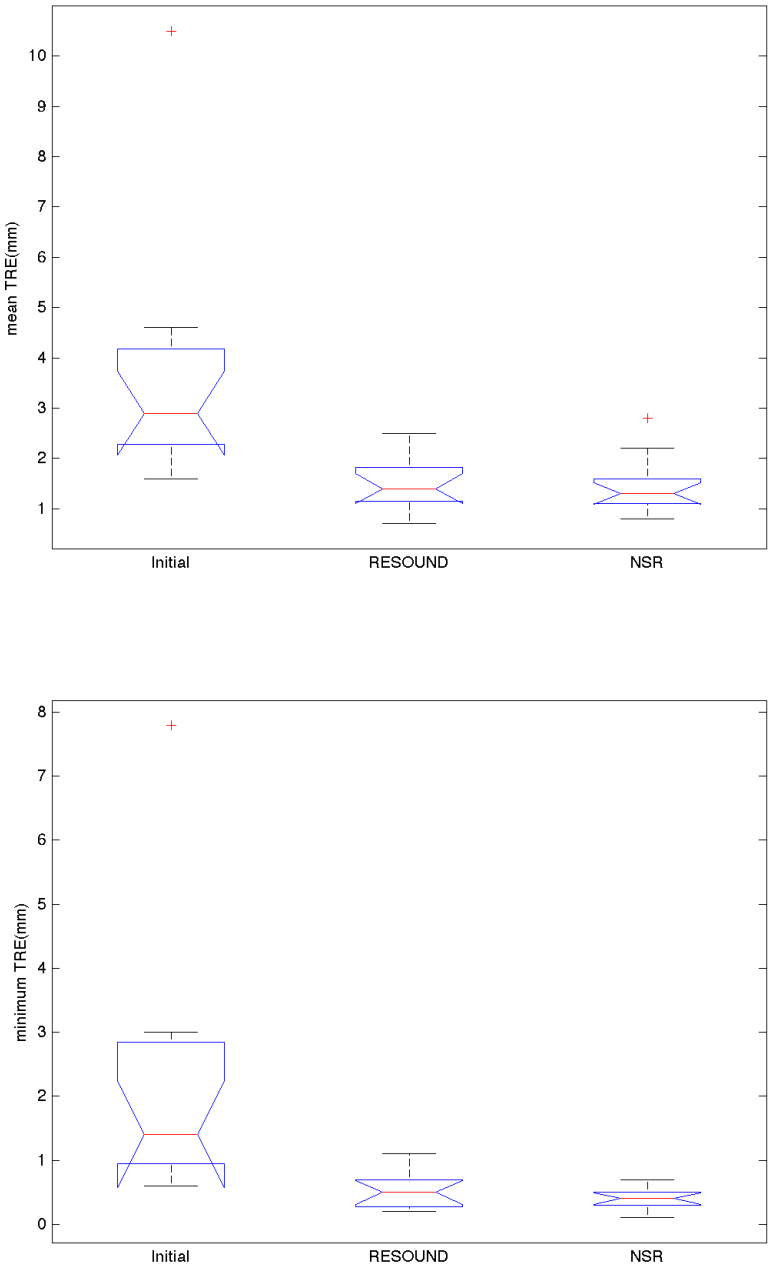

Figure 2.5: Boxplots of the mean (top) and minimum (bottom) TRE.

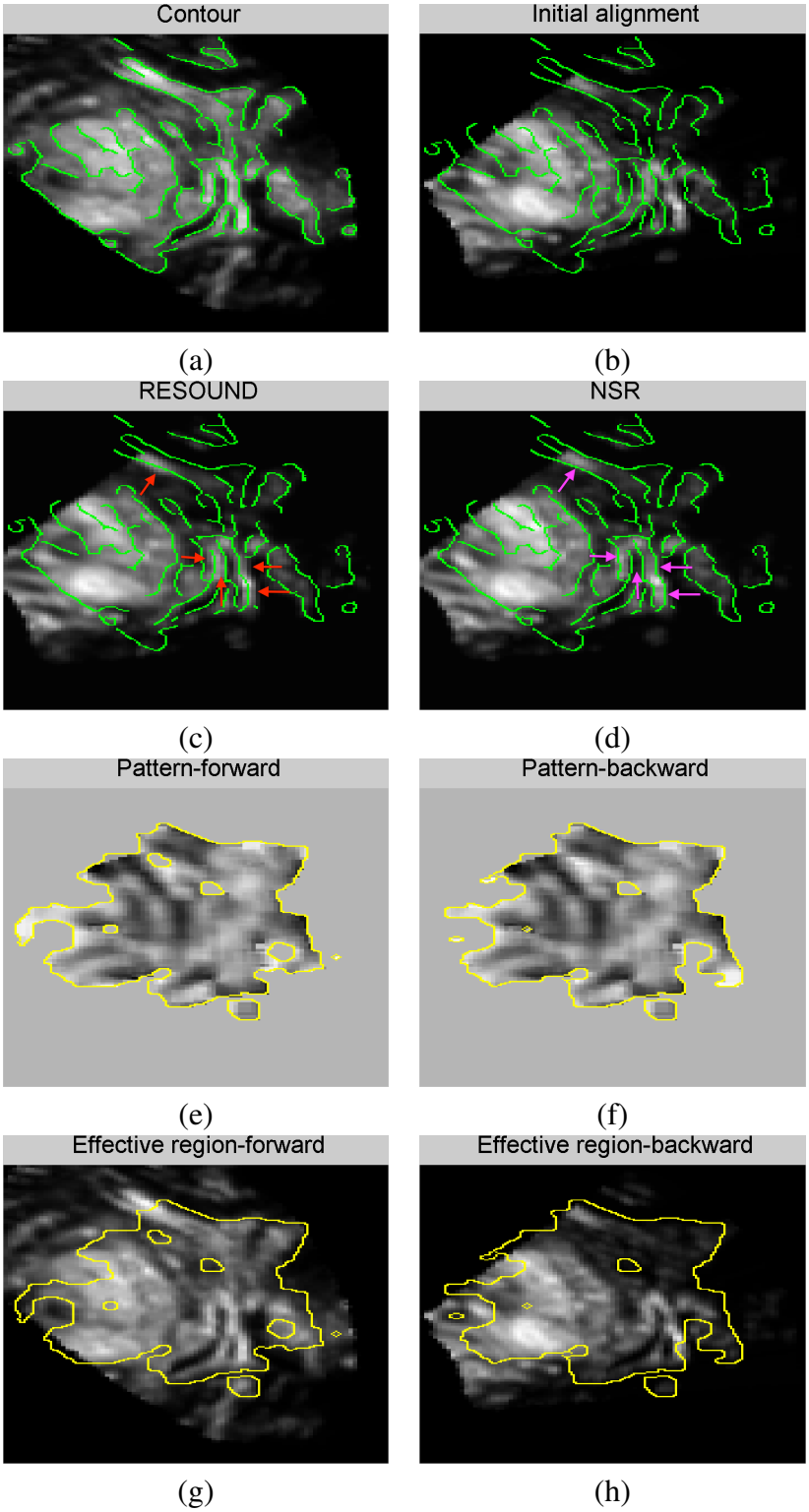

Figure 2.6: Registration results of Patient 2. Please refer to the text for details.

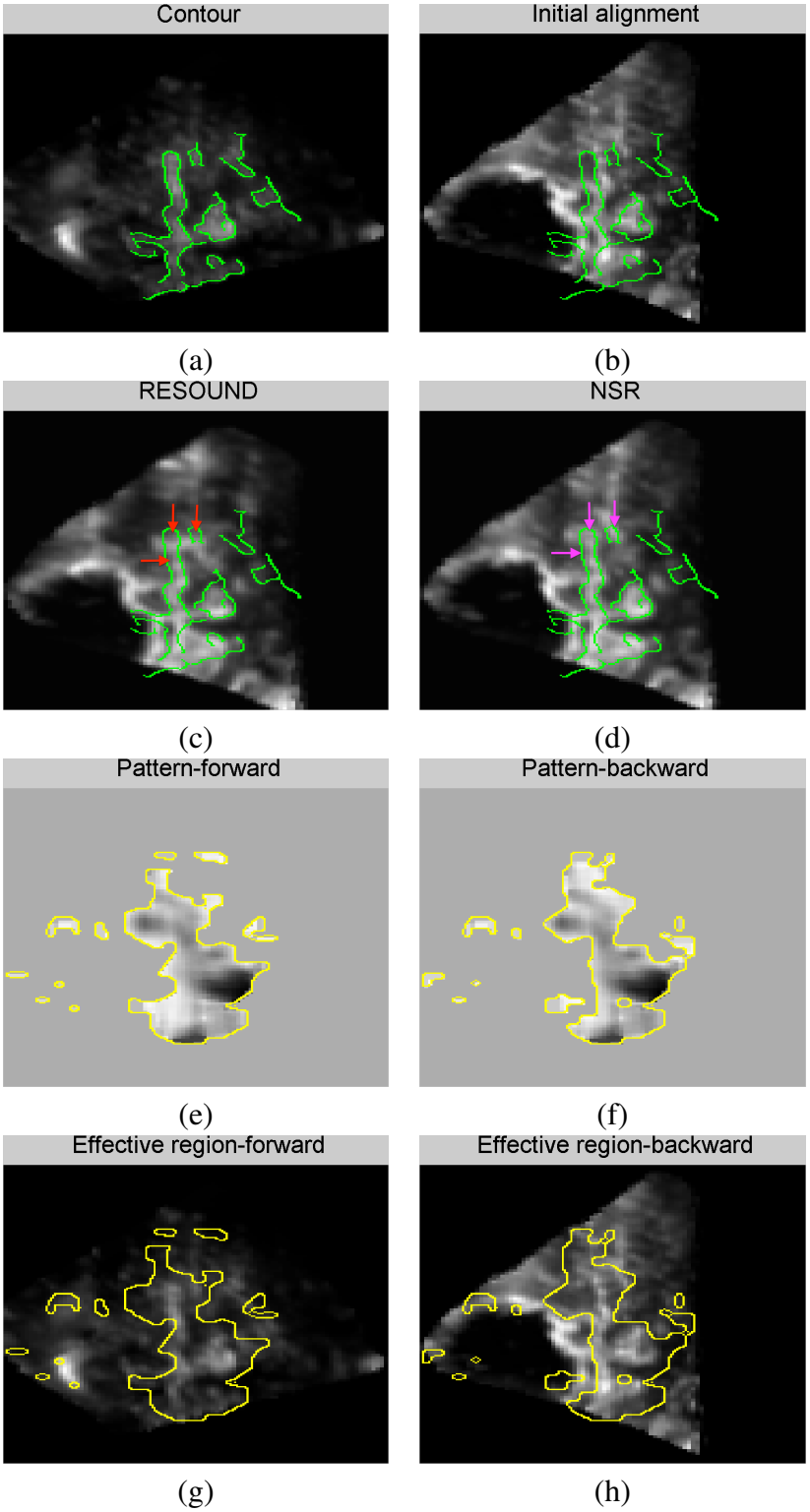

Figure 2.7: Registration results of Patient 4. Please refer to the text for details.

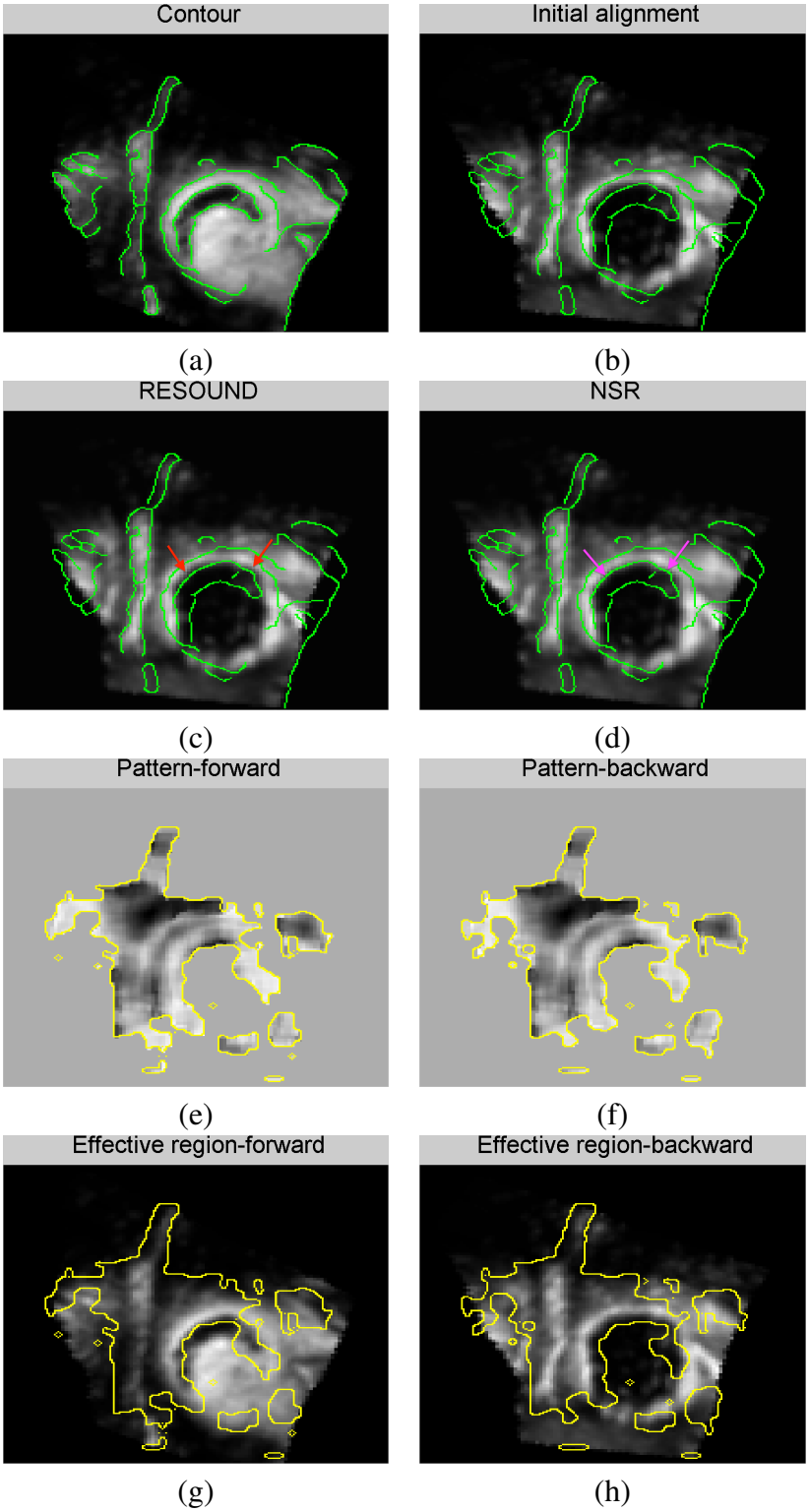

Figure 2.8: Registration results of Patient 10. Please refer to the text for details.

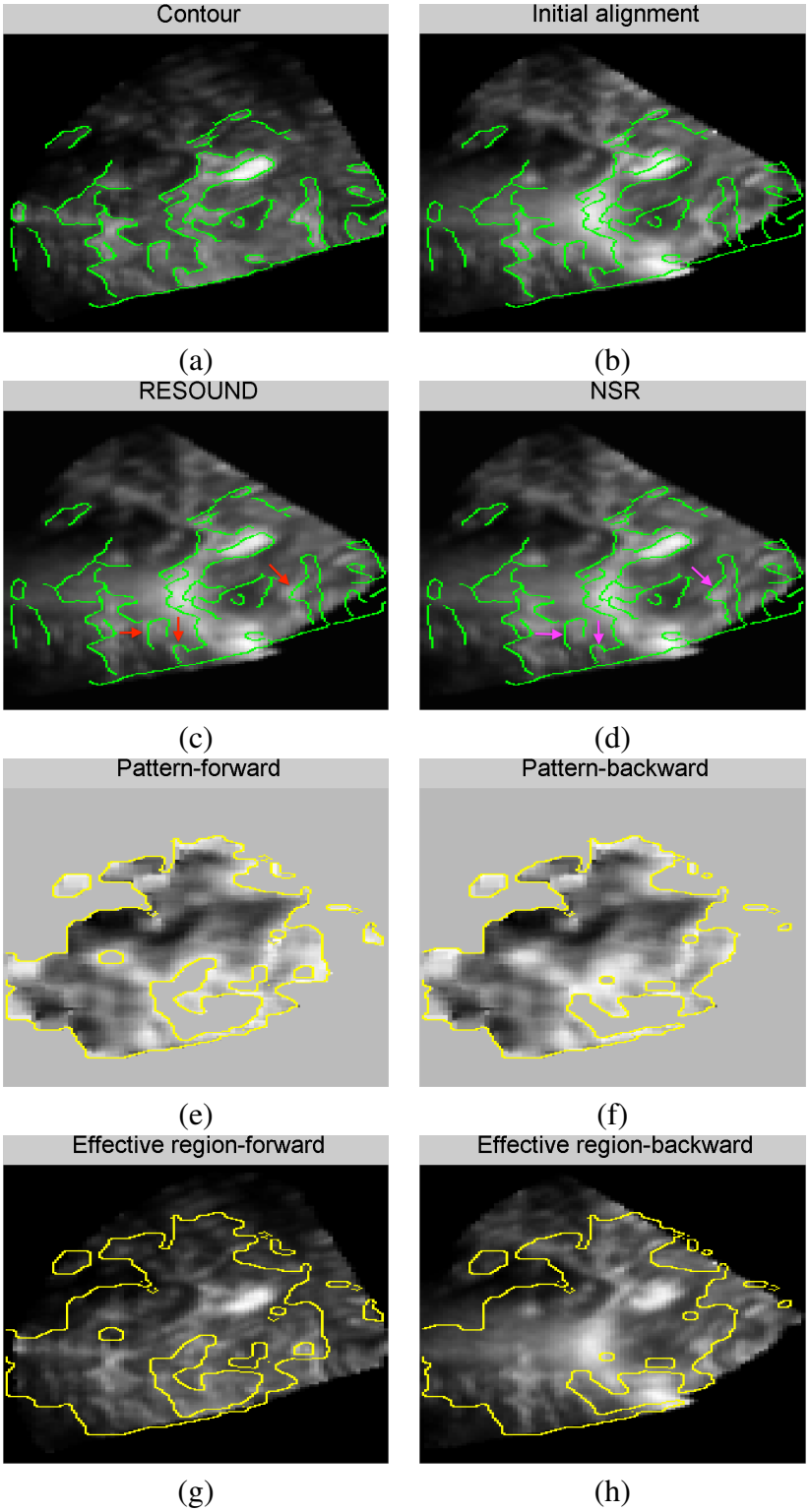

Figure 2.9: Registration results of Patient 13. Please refer to the text for details.

Chapter 3

Registration of Ultrasound Volumes in Prostate Radiotherapy

3.1 Introduction

Prostate motion is known to reduce the precision of prostate radiotherapy. This motion can be categorized into two types: intrafraction (during the fraction) and interfraction (between the fractions) [15]. Intrafraction motion of the prostate is mainly due to bladder filling and bowel motion while interfraction motion is caused by daily changes in patient position and posture, as well as variation in bowel or bladder filling. Interfraction motion, the focus of the current study, has the greatest potential to introduce large systematic errors into the treatment and is the largest contributor to prostate planning treatment volume (PTV) margins

required to compensate for geometrical motion [48]. Conventional solutions to interfraction motion include megavoltage X-ray portal imaging, kilovoltage X-ray imaging or cone-beam CT (CBCT) of bony anatomy and adjusting the patient's position according to the comparison of pre-treatment (simulation) and treatment images. This correction, however, may be inaccurate since the prostate can move with respect to bony anatomy [49].

Fiducial markers (FMs) implanted into the prostate may be used to overcome this limitation, these may be small metallic markers visible on x-ray imaging or electromagnetic transponders which can be localized using the Calypso system (Varian Medical Systems Inc., Paolo Alto, CA, USA). The implantation of markers, whilst straightforward, requires an additional procedure and the administration of prophylactic antibiotics [16]. Ultrasound imaging is non-invasive, allows direct visualization of the prostate and surrounding tissues in 4D (serial 3D imaging) and, unlike CBCT and portal imaging, can be applied to the correction of both interfraction and intrafraction motion [2].

The first generation Clarity system (Elekta AB. Stockholm, Sweden) used a 3-dimensional (3D) transabdominal ultrasound (TAUS) approach to image the prostate for interfraction motion estimation. A 3D transperineal ultrasound (TPUS) approach was introduced in 2012, and the Clarity Autoscan system provided continuous ultrasound imaging of the prostate for intrafraction motion estimation without affecting the radiation delivery [50]. The Clarity system uses manual comparison of a TPUS image acquired at simulation and a TPUS image acquired prior to treatment to calculate the couch shift necessary to correct for interfraction

motion. This requires the radiation therapist to scroll back and forth through the 3D volume, in two or three of the axial, sagittal and coronal planes, iteratively adjusting a matching contour (the reference position volume (RPV)), which can be time-consuming. Also, ultrasound is well known to be a user-dependent modality, which results in variations in image quality and observer errors; poor image quality can lead to large interobserver errors in estimated interfraction motion [51].

An automated registration of the simulation and treatment TPUS images would reduce the time required for interfraction motion correction and may potentially improve precision. Similar to commercially available image-guided radiotherapy softwares [49], results of the algorithm could be displayed to the radiation oncologist for visual inspection prior to couch correction. In the current study, an automatic registration algorithm, Prostate Registration Framework (PRF), which was trained using 2 3D TPUS images of an ultrasound prostate phantom and 20 3D TPUS images from 11 patients receiving Clarity Autoscan, was developed. Algorithm performance was evaluated using further 21 TPUS images from a total of 8 patients by comparison of the PRF with manual matching of landmarks (LMs) and Clarity-based estimation of interfraction motion performed by three observers.

3.2 Material and methods

3.2.1 Data acquisition

Clarity system

The Clarity Autoscan prostate radiotherapy workflow has been described in detail elsewhere [50, 52]. Briefly, the system used a 3D-swept array probe in a transperineal imaging configuration incorporating a convex transducer array with central frequency of 5MHz. For interfraction motion estimation, single 3D TPUS images with sweep angle 75° and maximum imaging depth 15cm were acquired in 0.5 seconds immediately prior to simulation CT and each treatment fraction. The probe was positioned on a base-plate, which was centered on the CT and treatment couches and indexed to allow the superior-inferior (SI) and anterior-posterior (AP) probe positions used at simulation to be reproduced during treatment. The location of the probe in the CT and treatment rooms was monitored using an optical tracking tool that was rigidly fixed to the probe and infrared cameras that were fixed to the ceilings of each room. A spatial calibration, performed using a dedicated phantom, was used to transform the position of voxels in the TPUS images to a location described using treatment co-ordinates, i.e., real-world coordinates relative to the treatment isocenter. The simulation TPUS was transferred from the ultrasound scanner to the Clarity Workstation and registered to the simulation CT. A RPV was defined by drawing a 3D contour of the prostate using the TPUS and CT images. The RPV and the simulation TPUS image ($\mathbf{V_s}$) were transferred back to the scanner. The

Autoscan probe was then repositioned during patient set-up and remained in place throughout treatment. A treatment TPUS image ($\mathbf{V_t}$) was acquired after patient set-up and, using the scanner's touch screen, the radiation therapist moved a copy of the RPV across the $\mathbf{V_t}$ in the SI, AP and left-right (LR) directions to indicate the position of the prostate in the $\mathbf{V_t}$. The Clarity system calculated the displacement between the RPV and the RPV copy to determine the couch shift required to correct for interfraction motion of the prostate. Two versions of the Clarity Acquisition software were used in this work: the research software, Anticosti and the clinical software.

Phantom data

Phantom data provided an idealized dataset with which to initially improve the performance of PRF. An anthropomorphic prostate phantom (Model 070S CIRS Inc. Norfolk, VA, USA) was CT scanned and imaged using Clarity Autoscan. One $\mathbf{V_s}$ was acquired in the CT room and two $\mathbf{V_t}$ were acquired in the treatment room with the phantom in two different positions relative to the probe. Images were exported from the Clarity workstation using the DICOM standard with the voxel size of 0.57 x 0.57 x 0.57 mm^3. Estimates of the motion between the $\mathbf{V_s}$ and two $\mathbf{V_t}$ were determined by one observer (EH) using the Clarity Review software.

Clinical data

Patients receiving radiotherapy for prostate cancer were imaged using Clarity Autoscan as part of a trial comparing Clarity motion estimation with implanted gold fiducial markers and portal imaging, and cone beam CT. The Surrey and SE coast NHS Research Ethics Committee approved the study [1]. For the current study, 41 $\mathbf{V_t}$ from the most recently treated 13 patients were chosen at random. There were between 1 and 5 images for each patient and 25 $\mathbf{V_t}$ were acquired from 8 patients who had received 3 implanted gold markers. The number of fiducial markers visible in each ultrasound image was scored by a radiation therapist (HM) who viewed the images using the Clarity workstation. Images were divided into a training set and a test set. All patient images and RPVs were exported using the DICOM standard for LM collection and PRF evaluation. Three Clarity interfraction motion estimates were obtained for each $\mathbf{V_t}$ by three observers (HM, AG and EH) using the Clarity Review software.

3.2.2 Landmarks collection

To validate the framework, the position of LMs, which was visible in both simulation and treatment TPUS images from the phantom and clinical data was collected by three observers (HZ, AG and EH). A minimum of 3 LMs within the prostate were collected for each image pair (simulation and treatment TPUS images) and the mean of the mean displacement of corresponding LMs for all three observers was used as the "silver standard ground truth".

[1] https://clinicaltrials.gov/ct2/show/NCT02388308

The Volume Viewer plugin for Image J (National Institutes of Health, Bethesda, Maryland) was used to visualize and determine the position of LMs in the axial, sagittal and coronal planes. Displacements were measured in millimeters in the LR, AP and SI directions. Fig. 3.1 gives an example of corresponding LMs, which were visible in both the simulation and treatment images.

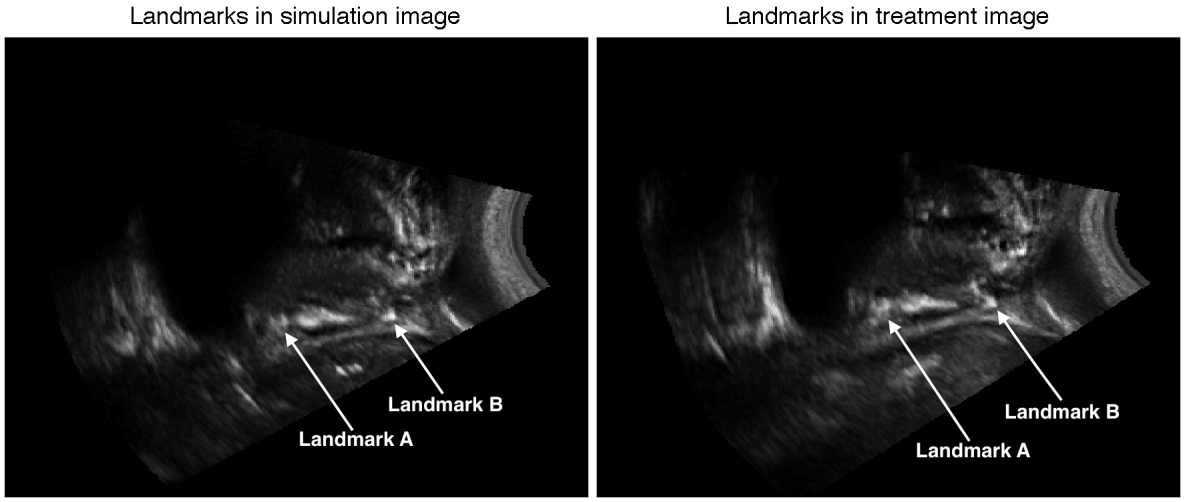

Figure 3.1: Corresponding landmarks in the simulation (left) and treatment (right) images

3.2.3 Prostate Registration Framework

The PRF was adapted from a previous registration framework, Non-rigid Symmetric Registration Framework, which was developed to register ultrasound images acquired pre- and post-neurosurgery for the purpose of estimating the residual tumor [39]. In the current study, rigid registration was used to calculate the displacement of the prostate between simulation and treatment images. Rigid registration without rotation was chosen because the Clarity

system only considers translational motion.

The outline of our framework is shown in Fig. 3.2 and we performed the following steps:

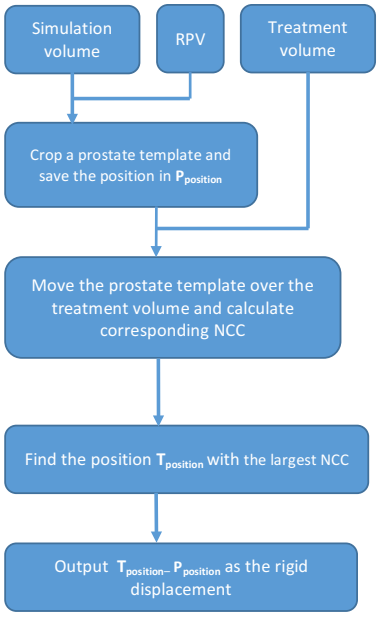

Figure 3.2: Outline of the PRF registration technique.

STEP 1: : The greatest extent of RPV in the x, y and z directions (corresponding to the SI, AP and LR directions) of the simulation volume $\mathbf{V_s}$ was determined.

STEP 2: The prostate template $\mathbf{V_p}$, a cuboid whose facets are defined by the greatest extent of RPV, was cropped from the simulation volume $\mathbf{V_s}$.

STEP 3: The coordinates of the vertex of the prostate template were saved in a matrix for subsequent calculation:

$$\mathbf{P_{position}} = [Px, Py, Pz] \tag{3.1}$$

where $\mathbf{P_{position}}$ is the position matrix and Px, Py, Pz are coordinates of the vertex of the prostate template $\mathbf{V_p}$ in the simulation volume $\mathbf{V_s}$.

STEP 4: The prostate template was used as a sliding-window and moved, voxel-by-voxel, through the treatment volume $\mathbf{V_t}$ and the corresponding similarity metric was calculated at each position. The start point of the iteration was $\mathbf{P_{position}}$ in the treatment volume and the search range was -R voxels to R voxels in the x, y, and z directions, where R is half of the search region size. Due to enhancing and shadowing artifacts in ultrasound images and changes of the insonification angle of the probe, the intensity of the same tissue in the prostate template and treatment volumes may vary. Normalized Cross Correlation (NCC) was used as the similarity metric, which is invariant to such affine distortions of intensity values. To increase the accuracy of the NCC calculation, the prostate template and corresponding region in the treatment volume were sub-divided into $\mathbf{N}$ non-overlapping patches (smaller volumes) [44] and the mean of NCC values of corresponding patches was used as the overall similarity. The NCC of $\mathbf{V_p}$ and the corresponding region in $\mathbf{V_t}$ was calculated as follows:

$$\rho_{\mathbf{i}} = \frac{\sum_{j=1}^{n}(\mathbf{V_{pi}}_j - \overline{\mathbf{V_{pi}}})(\mathbf{V_{ti}}_j - \overline{\mathbf{V_{ti}}})}{\sum_{j=1}^{n}(\mathbf{V_{pi}}_j - \overline{\mathbf{V_{pi}}})\sum_{j=1}^{n}(\mathbf{V_{ti}}_j - \overline{\mathbf{V_{ti}}})} \tag{3.2}$$

$$\mathbf{NCC} = \frac{\rho_{\mathbf{1}} + \rho_{\mathbf{2}} + \cdots + \rho_{\mathbf{i}} + \cdots + \rho_{\mathbf{N}}}{\mathbf{N}} \tag{3.3}$$

where $\mathbf{V_{pi}}$ and $\mathbf{V_{ti}}$ are patch $\mathbf{i}$ in $\mathbf{V_p}$ and $\mathbf{V_t}$ respectively, $\mathbf{V_{pi}}_j$ and $\mathbf{V_{ti}}_j$ are the intensity of pixel j in patch $\mathbf{i}$, $\overline{\mathbf{V_{pi}}}$ and $\overline{\mathbf{V_{ti}}}$ are the mean intensity of patch $\mathbf{i}$, $\rho_{\mathbf{i}}$ is the NCC of patch $\mathbf{i}$, $\mathbf{N}$ is the number of patches in $\mathbf{V_p}$ and n is the number of pixels in each patch.

STEP 5. The voxel with the maximum NCC was located and the rigid displacement is calculated by subtracting $\mathbf{P_{position}}$ from its coordinates $\mathbf{T_{position}} = [Tx, Ty, Tz]$, where $\mathbf{T_{position}}$ is the position matrix of the vertex of the corresponding region in the treatment volume $\mathbf{V_t}$.

$$\mathbf{D_{rigid}} = \mathbf{T_{position}} - \mathbf{P_{position}} \tag{3.4}$$

where $\mathbf{D_{rigid}}$ is the rigid deformation field from $\mathbf{V_p}$ to $\mathbf{V_t}$.

STEP 6: The prostate template $\mathbf{V_p}$ was translated by $\mathbf{D_{rigid}}$ to allow a visual check of the alignment with the treatment volume $\mathbf{V_t}$.

Hierarchical registration from coarse to fine levels was used to reduce the computation time and avoid getting trapped in local minima.

3.2.4 Framework optimization

Two phantom datasets and 20 clinical datasets from 11 patients formed the training data and were used to optimise the framework. The phantom data was an idealized simulation input because it contained no shadowing or deformation artifacts and provided a good initial test of the framework. The clinical data provided a realistic environment in which to optimize the framework and was used to determine the following parameters: the search region size R, the number of patches $\mathbf{N}$ and the levels of hierarchical registration. Optimization was performed by iteratively adjusting these parameters and calculating the median PRF error (see below) for each parameter set. R was varied between 30 voxels (11.54mm) and half of the whole treatment volume, in increments of 10 voxels. N was varied to be 1, 2, 4 and 8, and 2 and 3 levels of hierarchical registration were tested.

3.2.5 Registration error analysis

For each treatment image $\mathbf{V_t}$, the mean LM displacement estimates of the three observers were used as the ground truth. Three types of errors were defined:

(1) PRF error: The difference between the PRF displacement and the ground truth displacement.

(2) Clarity error: The difference between the mean Clarity displacement of the three observers and the ground truth displacement.

(3) LM error: The difference between the LM displacement of a single observer and the

ground truth displacement.

The proposed clinical implementation of PRF will provide an automatic estimate of the new position of the prostate. The new position can be displayed to the radiation therapist for manual assessment allowing large PRF errors (if there are) to be manually corrected prior to couch correction and treatment. The magnitude of PRF error that may be easily detected by a radiation therapist was defined as three times the standard deviation of the Clarity errors of both training and test data sets, and was used as an error exclusion threshold in the following analysis.

The accuracy and precision of PRF was defined as the median and interquartile range of the absolute PRF errors, excluding all PRF errors greater than the exclusion threshold. The accuracy and precision of Clarity was defined as the median and interquartile range of the absolute Clarity errors. To assess the performance of PRF, the distribution of PRF errors was compared to the distribution of LM errors and Clarity errors using Wilcoxon rank sum test to test for differences in medians and using box-plots for differences of overall distribution.

3.3 Results

3.3.1 Prostate Registration Framework parameters

After optimization of PRF using the training data, the following parameters gave the best performance, i.e. the smallest PRF errors: a search region size R of 60 pixels (34.62mm)

anchored at the vertex of the RPV in $\mathbf{V_t}$, $\mathbf{N} = 8$ patches and 2 levels hierarchical registration. The computation time for PRF was around 60 seconds on a 3GHz processor per image pair.

3.3.2 Performance of PRF

A total of 20 training and 21 test images from a total of 13 patients were used in the analysis. 29 images were acquired with the research software (AntiCosti) and 12 images were acquired with the clinical software. Three times the standard deviation of Clarity errors was approximately 10 mm, which was selected as the PRF error exclusion threshold. 5 images of 2 patients were excluded from the analysis because of large PRF errors (greater than 10 mm). The Wilcoxon rank sum test results between the absolute LM, absolute Clarity and absolute PRF errors are shown in Table 3.1 The median and the interquartile range of the absolute LM, absolute Clarity and absolute PRF errors for training and test data, are given in Table 3.2. From the comparison between the Clarity and PRF errors, we can find that PRF shows much smaller error values in all directions of training data and two directions of test data.

The distribution of the LM, Clarity and PRF errors for training and test data are shown using box-plots in Fig. 3.5 for the LR, AP and SI directions respectively. It shows that the PRF errors are more concentrated at zero compared with the Clarity errors. Two qualitative examples of the PRF displacement estimation are given in Figs. 3.3, 3.4. Within each patient's result, in (a) the initial PRV contour is overlaid on the corresponding frame of $\mathbf{V_s}$ and in (b) the RPV is overlaid on the corresponding frame of $\mathbf{V_t}$ to show the misalignment of the RPV with

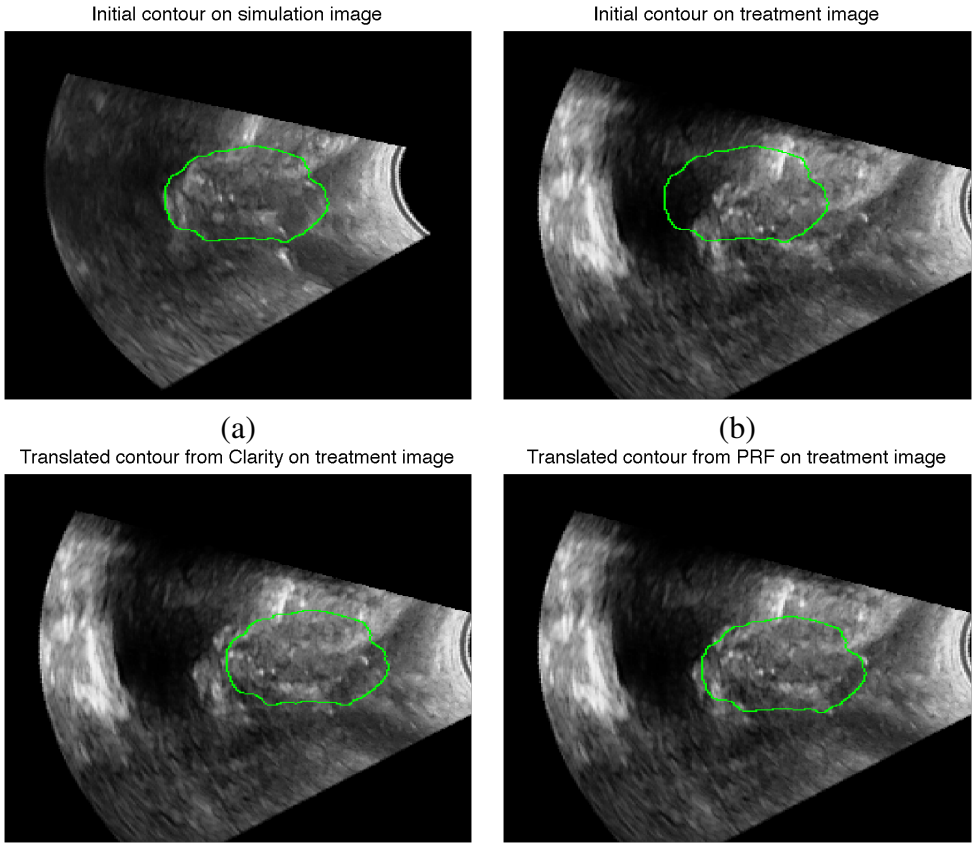

Figure 3.3: Registration results of Patient 1 T1. Please refer to the text for details.

the prostate. In (c) the RPV is translated by the Clarity displacement estimation. In (d) the RPV is deformed by the PRF displacement to compare with the Clarity result, which shows PRF can provide more accurate alignment of the prostate region in simulation and treatment images.

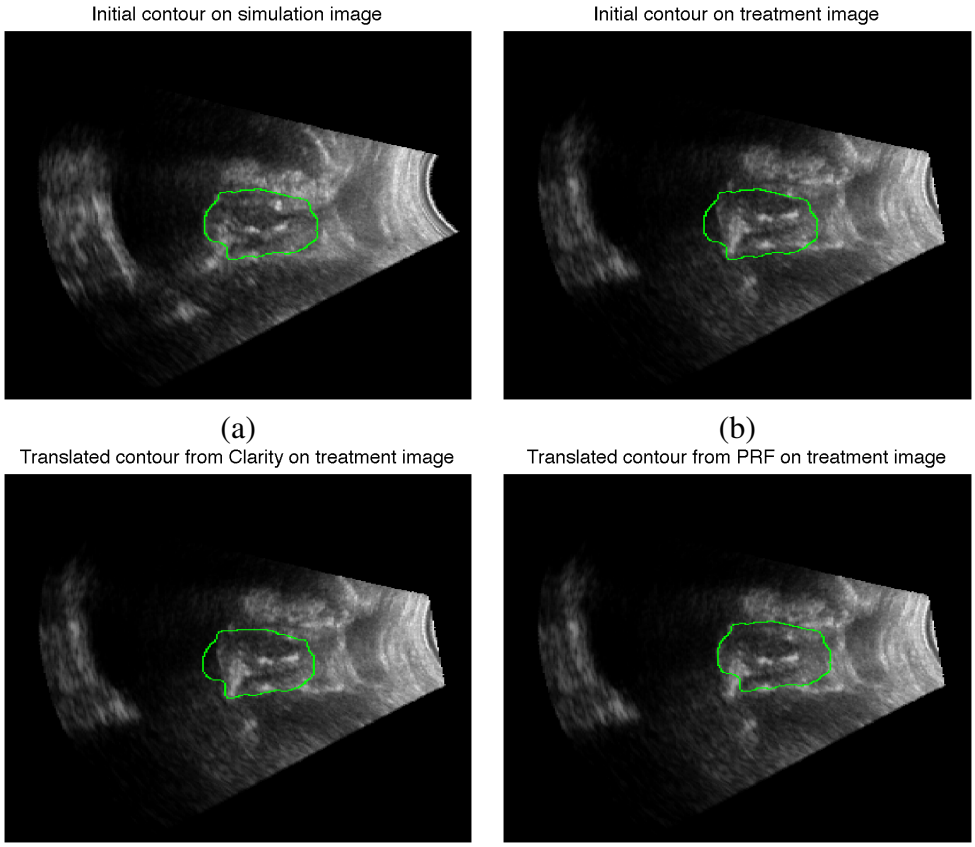

Figure 3.4: Registration results of Patient 2 T1. Please refer to the text for details.

3.4 Discussion

Registration of ultrasound volumes is an active field of research with numerous new advances. Ultrasound registration methods can be categorized into feature-based [28–30] and intensity-based [31–35]. Feature-based methods first find corresponding points in the two ultrasound volumes, and then use these correspondences to find registration transformation.

Datasets/ Results	Clarity error vs. LM error						PRF error vs. LM error						PRF error vs. Clarity error					
	Decision			*p*-value			Decision			*p*-value			Decision			*p*-value		
	X	Y	Z	X	Y	Z	X	Y	Z	X	Y	Z	X	Y	Z	X	Y	Z
Training data	0	0	0	0.3421	0.7347	0.4205	1	0	1	0.0042	0.8198	0.0035	1	0	1	0.0040	1	0.0215
Test data	0	0	0	0.7040	0.1120	0.1749	0	0	1	0.8829	0.2092	0.0044	0	0	1	0.5324	0.5324	0.0105

Table 3.1: Wilcoxon rank sum tests for training and test data. Decision indicates the test decision and *p*-value shows the *p*-value of two-sided Wilcoxon rank sum tests.

Datasets/ Results	Landmark error			Clarity error			PRF error		
	X	Y	Z	X	Y	Z	X	Y	Z
Training data	0.4(0.2-0.8)	0.6(0.3-1.0)	0.6(0.3-1.2)	1.8(1.0-3.2)	1.1(0.9-3.4)	2.5(0.9-4.7)	0.7(0.3-1.3)	0.8(0.4-1.4)	1.0(0.5-1.4)
Test data	0.6(0.3-1.4)	0.6(0.2-0.9)	0.6(0.2-1.0)	0.9(0.5-3.0)	1.3(0.4-2.8)	1.8(0.9-4.5)	1.3(0.5-2.8)	0.9(0.5-1.9)	1.0(0.4-1.7)

Table 3.2: Comparison of Landmark, Clarity and PRF errors of training and test data in the x, y and z (SI, AP and LR) directions. In each cell, the values represent median (25th percentile - 75th percentile) of the errors.

Intensity-based methods rely on similarity metrics such as NCC [32, 33, 35], mutual information [34], or phase differences [31]. Another categorization can be made based on transformation, which can be rigid [29, 31, 32, 34, 35] or deformable [28, 30, 33]. Rigid registration has a much faster speed whereas deformable registration usually has significantly more degrees of freedom.

In this study, only translation was considered in rigid registration since there were not enough LMs in the prostate region of simulation and treatment volumes and only translation displacement was calculated in Clarity. There may be rotation in the prostate region of some patients' images, which renders our alignment inaccurate. Therefore an affine or deformable registration framework with more degrees of freedom will be more suitable for our study as long as there are enough LMs for measurement.

3.5 Conclusion

In this work, an automatic registration framework PRF was developed to calculate the displacement of the prostate between simulation and treatment TPUS images and further increase the accuracy of prostate radiotherapy. Rigid registration was deployed and its result was compared with the Clarity matching and LMs matching. NCC, which is invariant to affine distortion of intensity values was selected as the similarity metric. Training and test data from a phantom and 13 patients were tested to optimize and validate PRF. The results show that PRF can accurately calculate the displacement of the prostate between simulation and treatment images and further provides the reposition of the prostate in treatment images efficiently and accurately. PRF outperforms Clarity in two aspects: being a fully automatic framework eliminating interobsever errors and providing more accurate displacements.

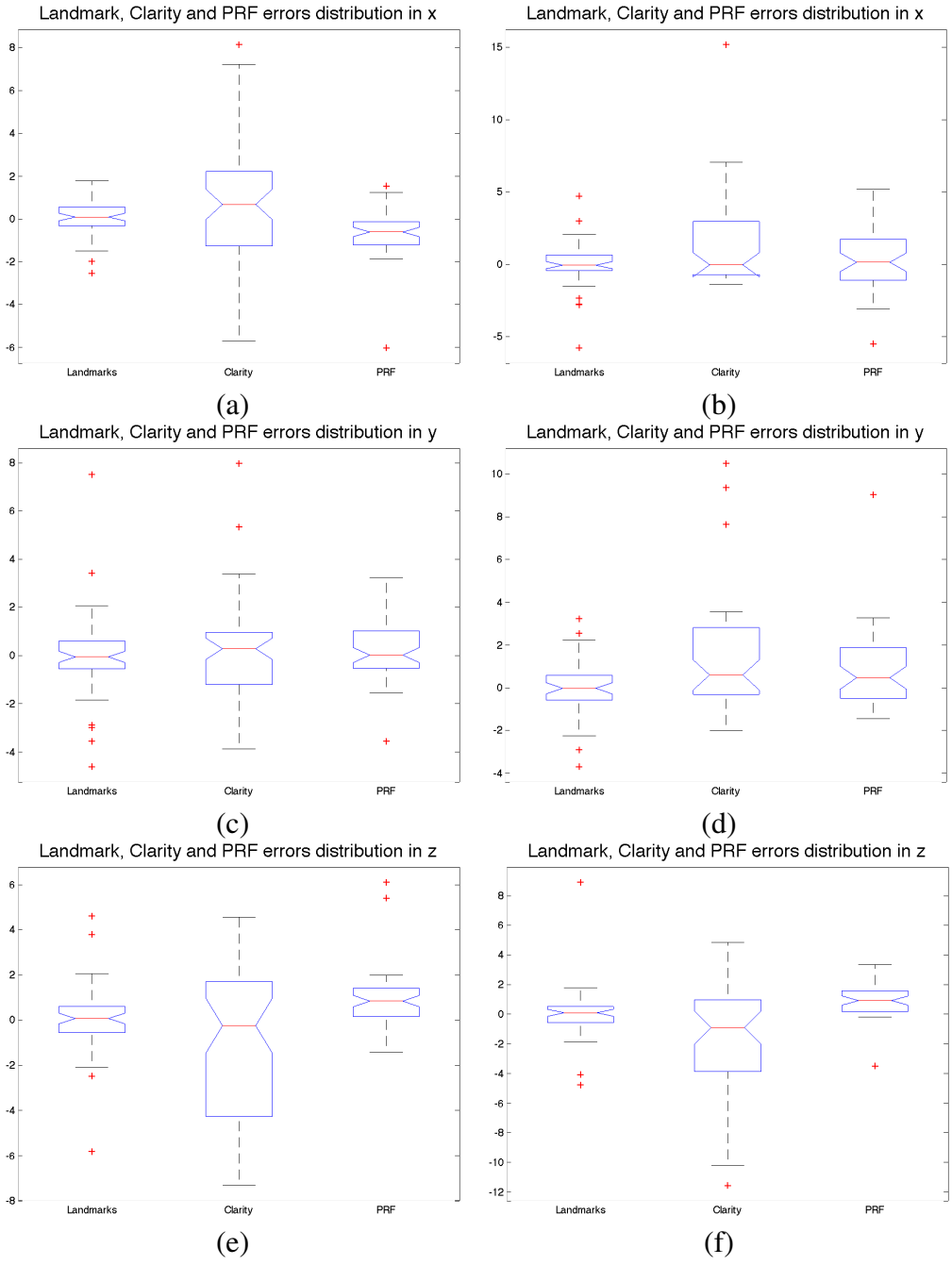

Figure 3.5: Box-plots showing the distribution of Landmark, Clarity and PRF errors of training ((a), (c), (e)) and test ((b), (d), (f)) data in the x, y and z (SI, AP and LR) directions.

Chapter 4

Conclusion and Future Work

4.1 Conclusion

US imaging becomes very popular these days. Compared with MRI, it is convenient, significantly less expensive and particularly ideal for soft tissue. These advantages and the non-invasive attribute make US imaging very useful in diagnosis and treatment. The techniques developed in this thesis further improve the potential of the US imaging modality. Image registration aligns different images into one coordinate system. In classical registration methods, the moving image is deformed to the fixed image, rendering the deformation not necessarily invertible, and can cause physically implausible folds or ruptures. Symmetric and inverse-consistent methods have been introduced to solve the asymmetry and reduce the bias. The selection of similarity metric is significantly important in a registration framework,

depending on the imaging modality and other conditions.

In this thesis, we first demonstrate a robust deformable registration framework for accurate alignment of pre- and post-resection US volumes in neurosurgery. NCC is utilized as the similarity metric because of its invariance to affine distortions of intensity values. ESM is exploited to optimize the regularized cost function to achieve fast and robust registration. A symmetric and inverse-consistent approach is used to generate realistic deformation fields. Moreover, an outlier detection method is proposed and utilized to identify and locate non-corresponding regions. The improved registration results are aroused by the unbiased deformation model and more efficient optimization. Then based on this framework, we propose an automatic registration algorithm PRF to calculate the displacement of the prostate between simulation and treatment images. PRF is trained using 2 3D TPUS images of an ultrasound prostate phantom and 20 3D TPUS images from 11 patients receiving Clarity Autoscan. Algorithm performance is evaluated using further 21 TPUS images from a total of 8 patients by comparison of the PRF with manual matching of LMs and Clarity-based estimation of inter-fraction motion performed by three observers. PRF outperforms Clarity in two aspects: being a fully automatic framework eliminating interobsever errors and providing more accurate displacements.

4.2 Future work

In Chapter 2, we demonstrate NSR for alignment of pre- and post-resection ultrasound volumes in neurosurgery. Considering the practical requirements of neurosurgery, our framework still needs to be improved in terms of speed. A real-time performance is significantly important in image-guided neurosurgery. One improvement can be made on the optimization part since even though ESM method can achieve a cubic convergence rate, it imposes a high demand of computation on the processor. In the future work, we will try to find more efficient optimization methods with a similar convergence rate. An alternative solution is the parallel implementation of NSR, which can be achieved with the help of GPU computation. We only test our deformable registration framework on tumor images in neurosurgery. However, the application of our framework is not limited to just this one aspect. In the future research we will try to implement our technique on detection of other types of tumors and other image-guided treatments.

In Chapter 3, a rigid registration framework for accurate calculation of the displacement of the prostate between simulation and treatment images is demonstrated. One problem in this work is we only utilize translation in rigid registration since there are not enough LMs in the prostate region of simulation and treatment images. However, the prostate region can be rotated in some patients' treatment images, which renders our registration inaccurate. Therefore an affine or deformable registration framework with more degrees of freedom will be more suitable for our study as long as there are enough LMs for measurement.

Appendix A

Supplementary Material

To further demonstrate the effectiveness of our registration framework and our outlier detection algorithm, pre- and post-registration alignments of images of the remaining 9 patients are shown in Figs. A.1, A.2, A.3, A.4, A.5, A.6, A.7, A.8 and A.9. The outlier detection algorithm identifies and locates outliers accurately, and therefore the alignment after NSR (d) is significantly improved compared with RESOUND (c). Parts (e) and (f) show "Effective Region" for both directions, and parts (g) and (h) are the overlay of the contour of "Effective Region" on the corresponding frame of the volume. It is clear that low SNR and non-corresponding regions are not in the "Effective Region".

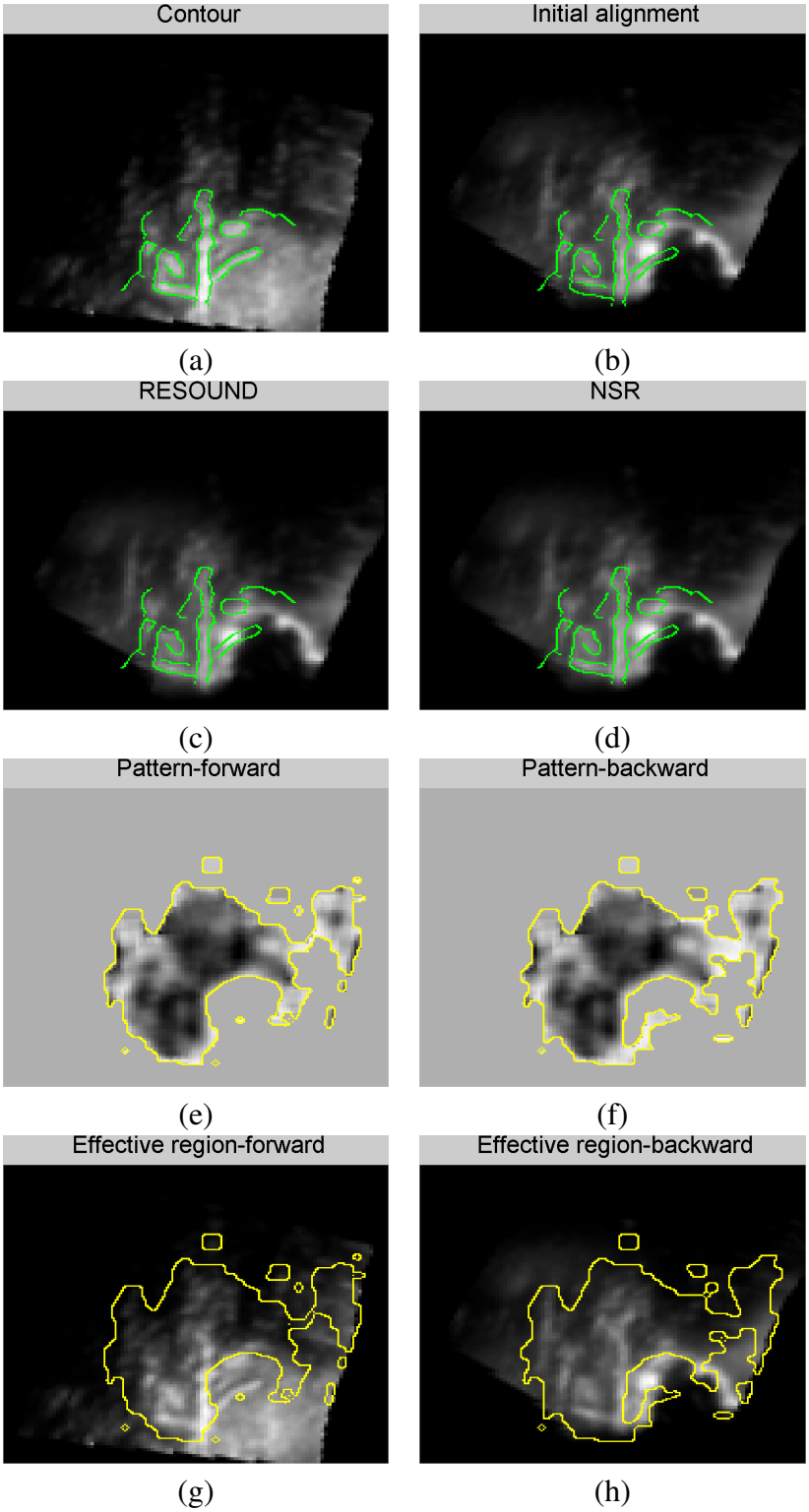

Figure A.1: Registration results of Patient 1. Please refer to the text for details.

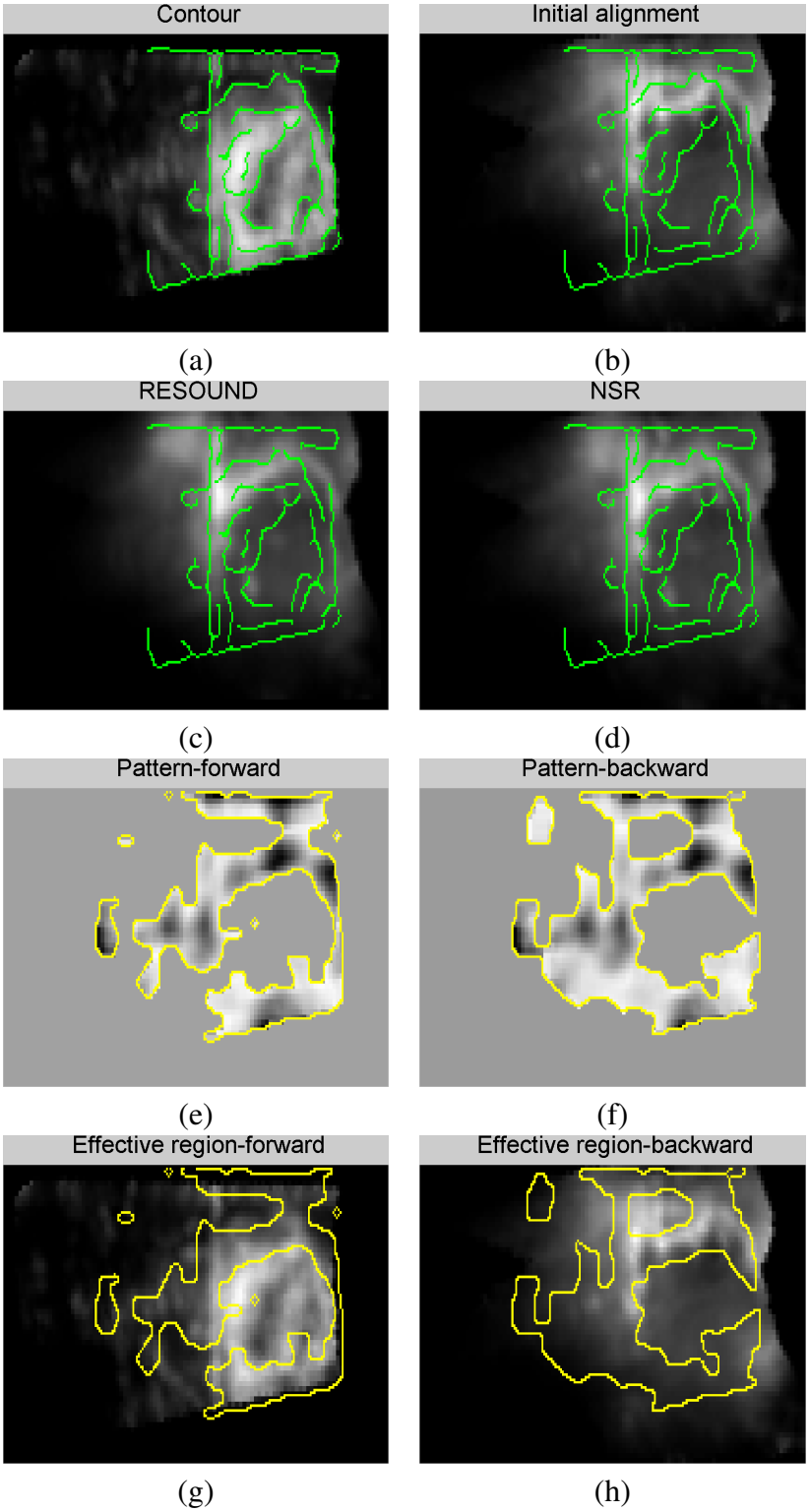

Figure A.2: Registration results of Patient 3. Please refer to the text for details.

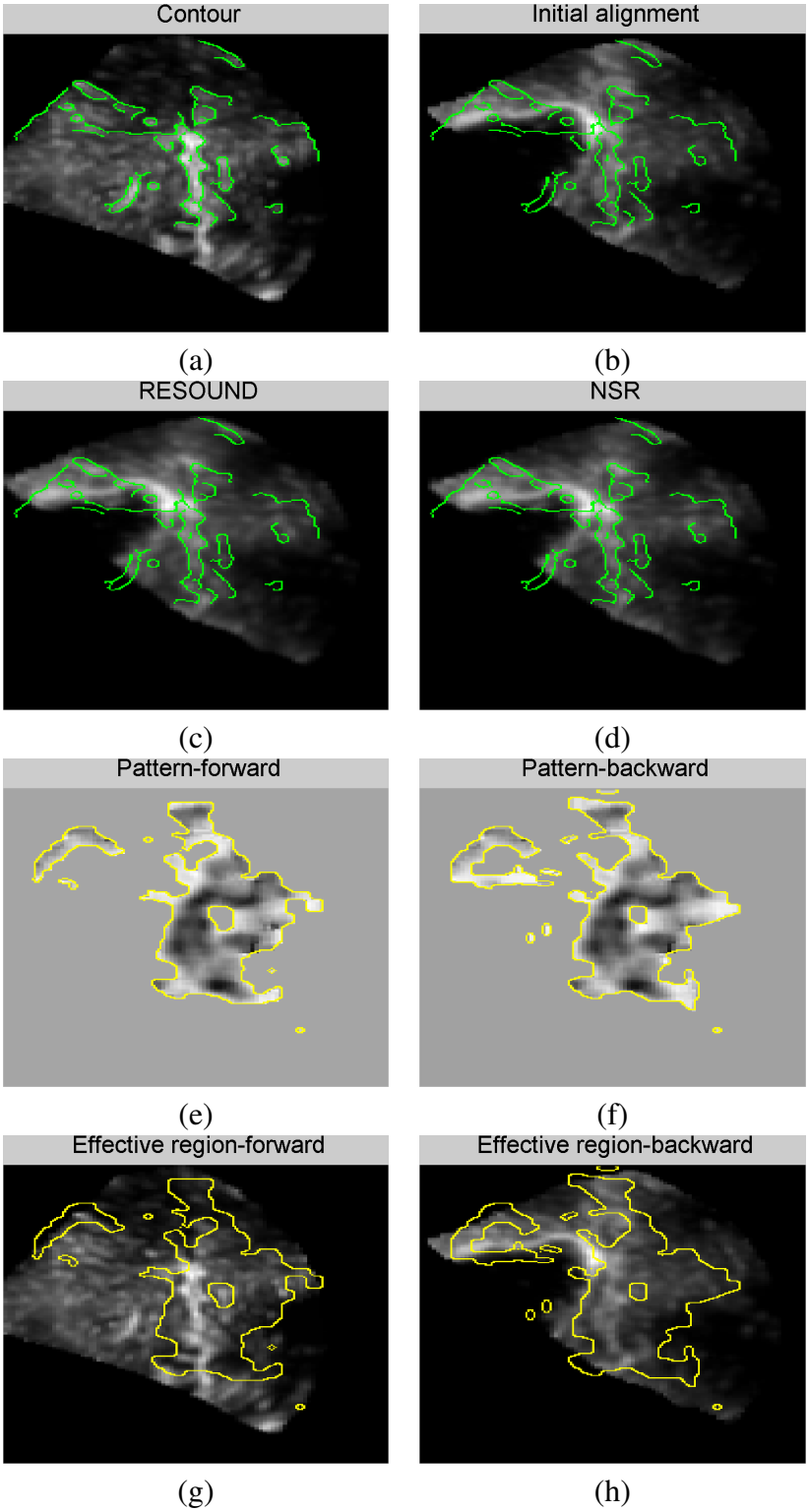

Figure A.3: Registration results of Patient 5. Please refer to the text for details.

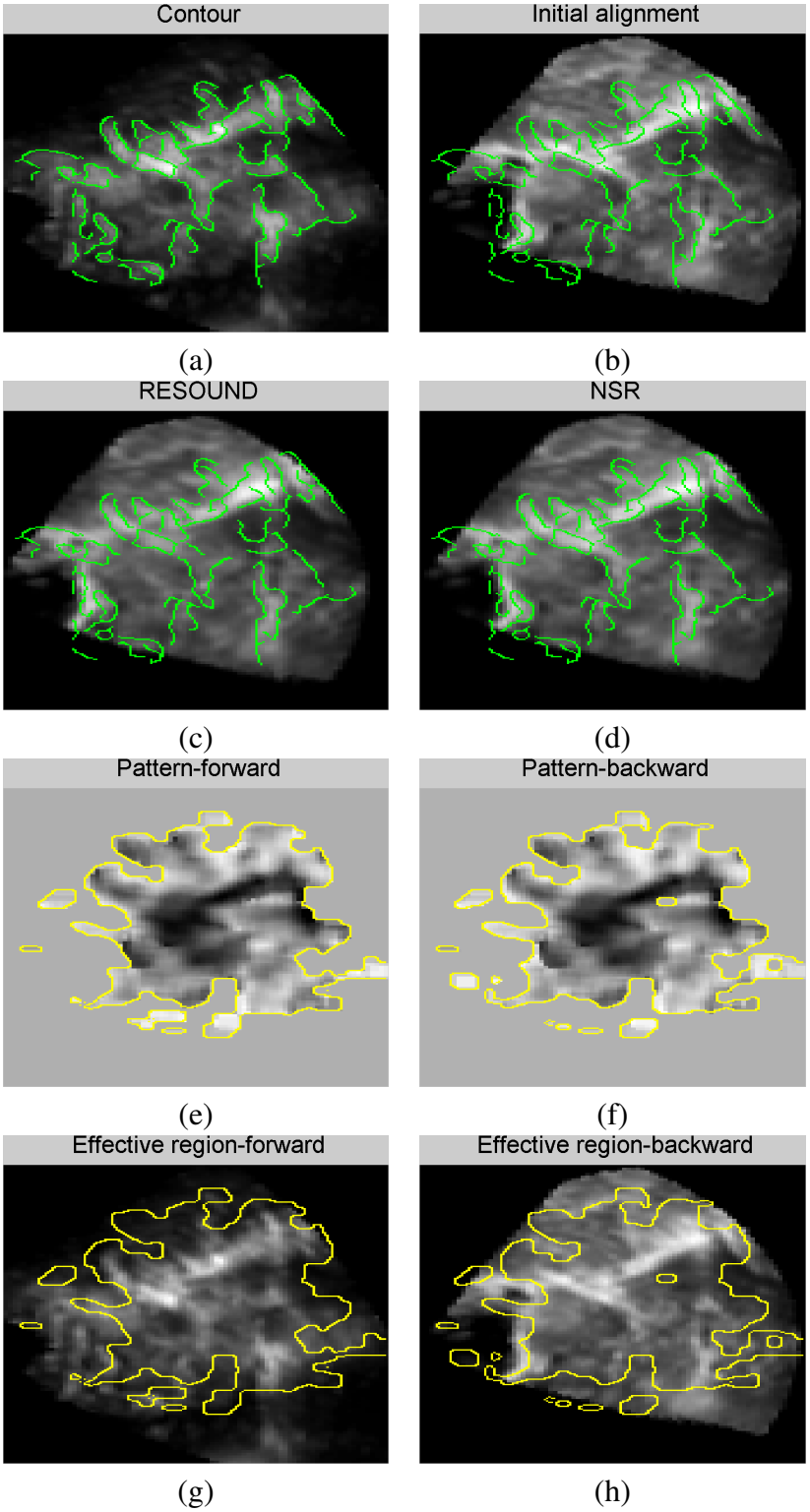

Figure A.4: Registration results of Patient 6. Please refer to the text for details.

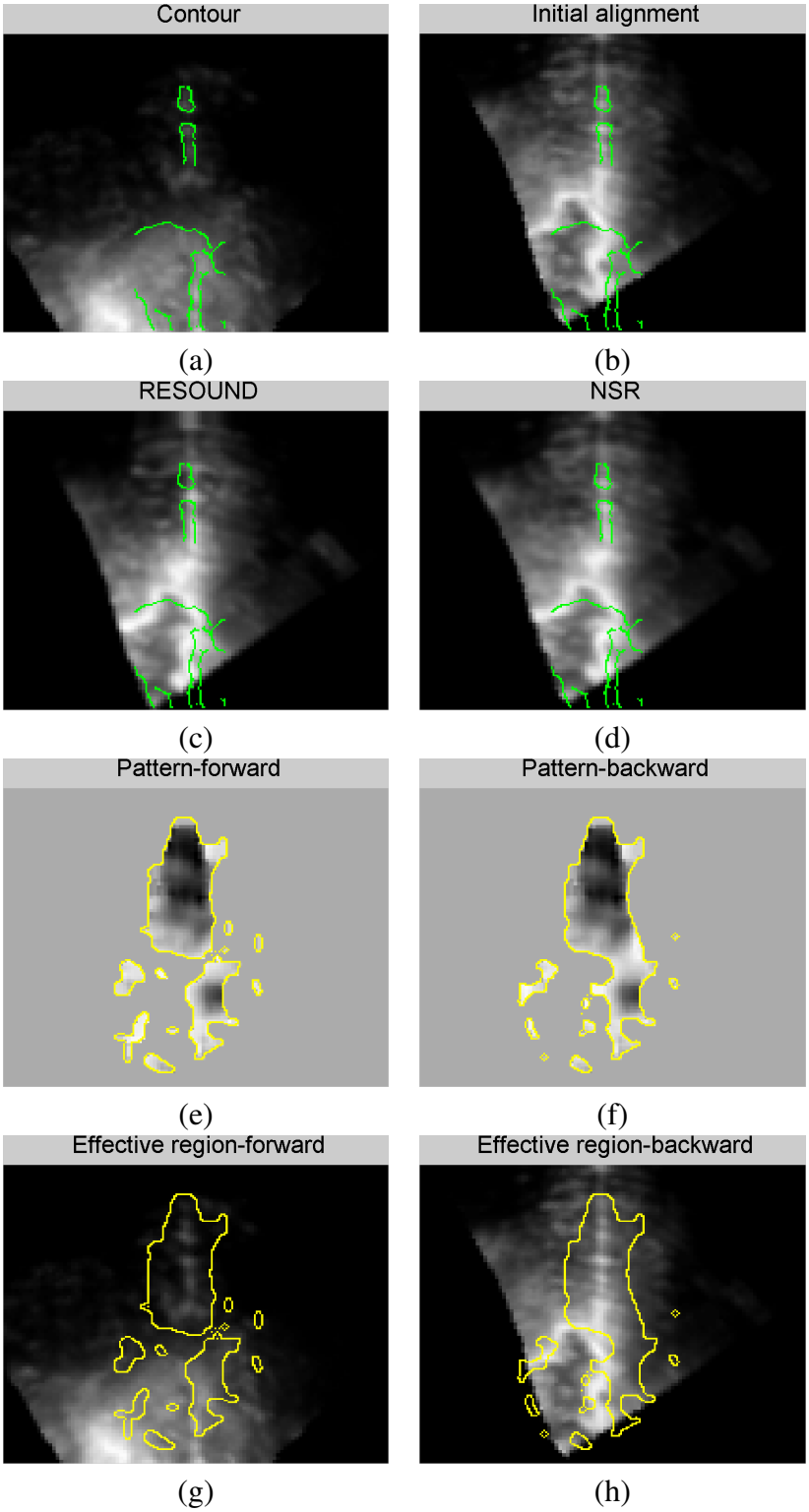

Figure A.5: Registration results of Patient 7. Please refer to the text for details.

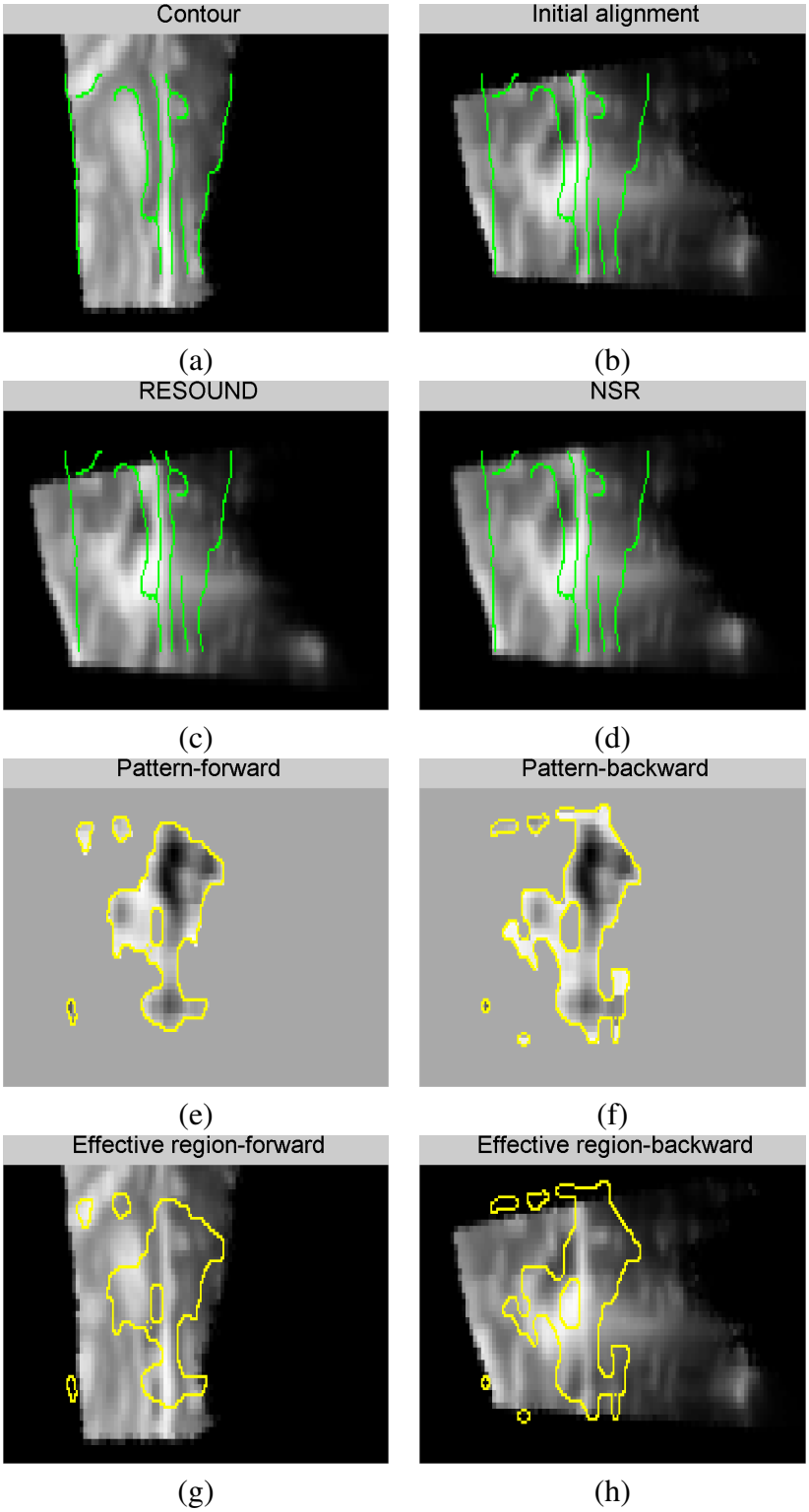

Figure A.6: Registration results of Patient 8. Please refer to the text for details.

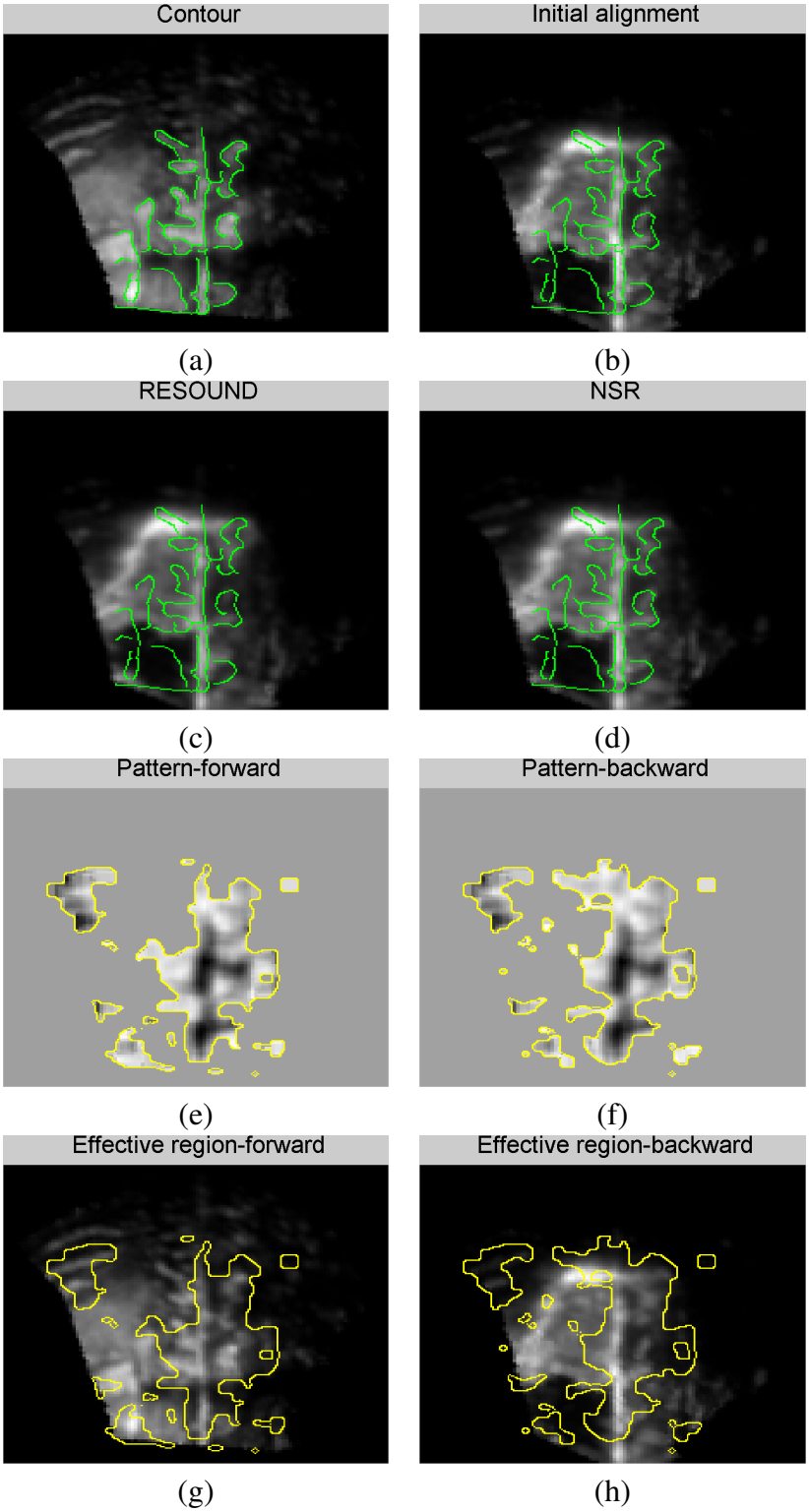

Figure A.7: Registration results of Patient 9. Please refer to the text for details.

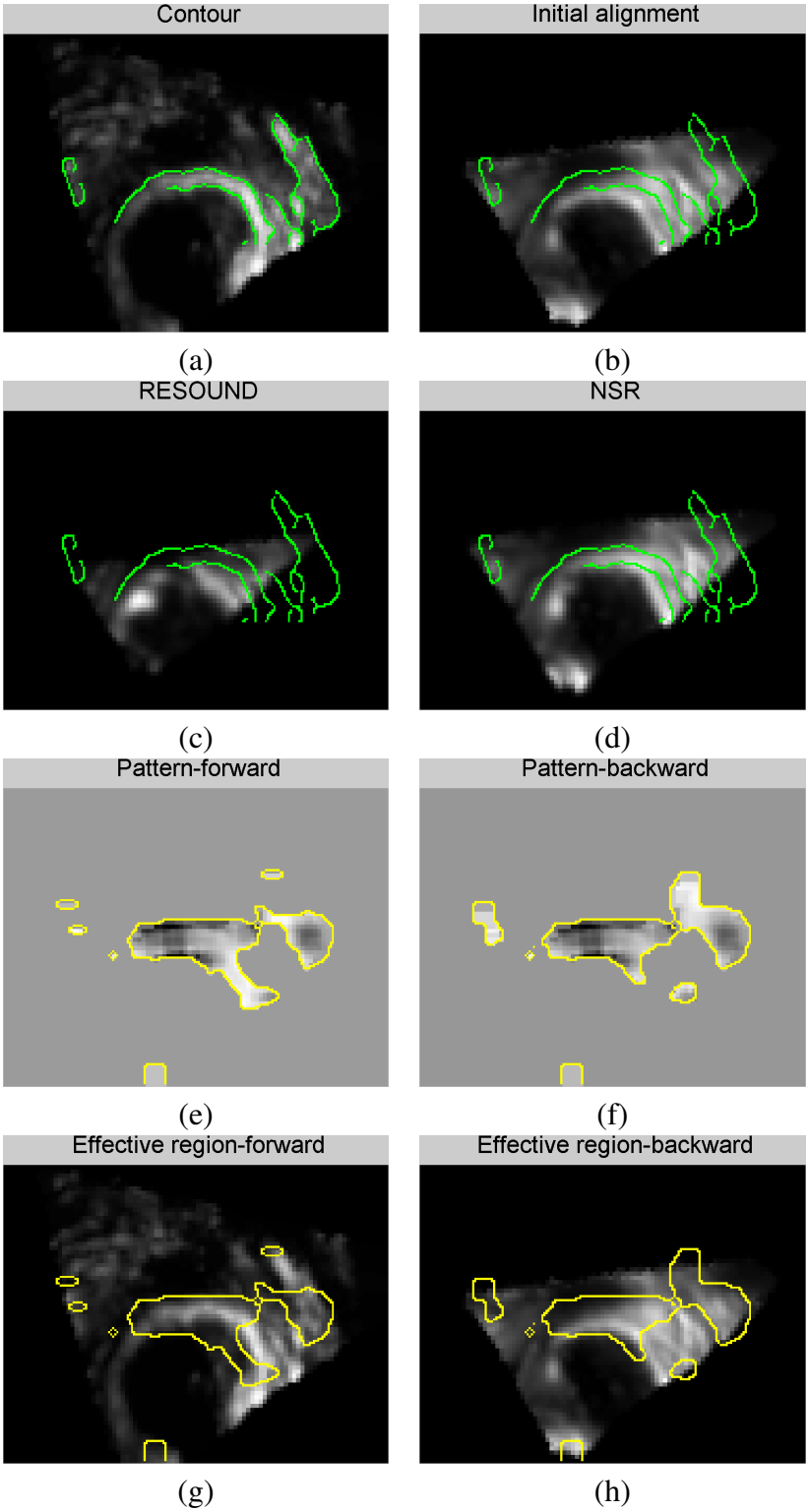

Figure A.8: Registration results of Patient 11. Please refer to the text for details.

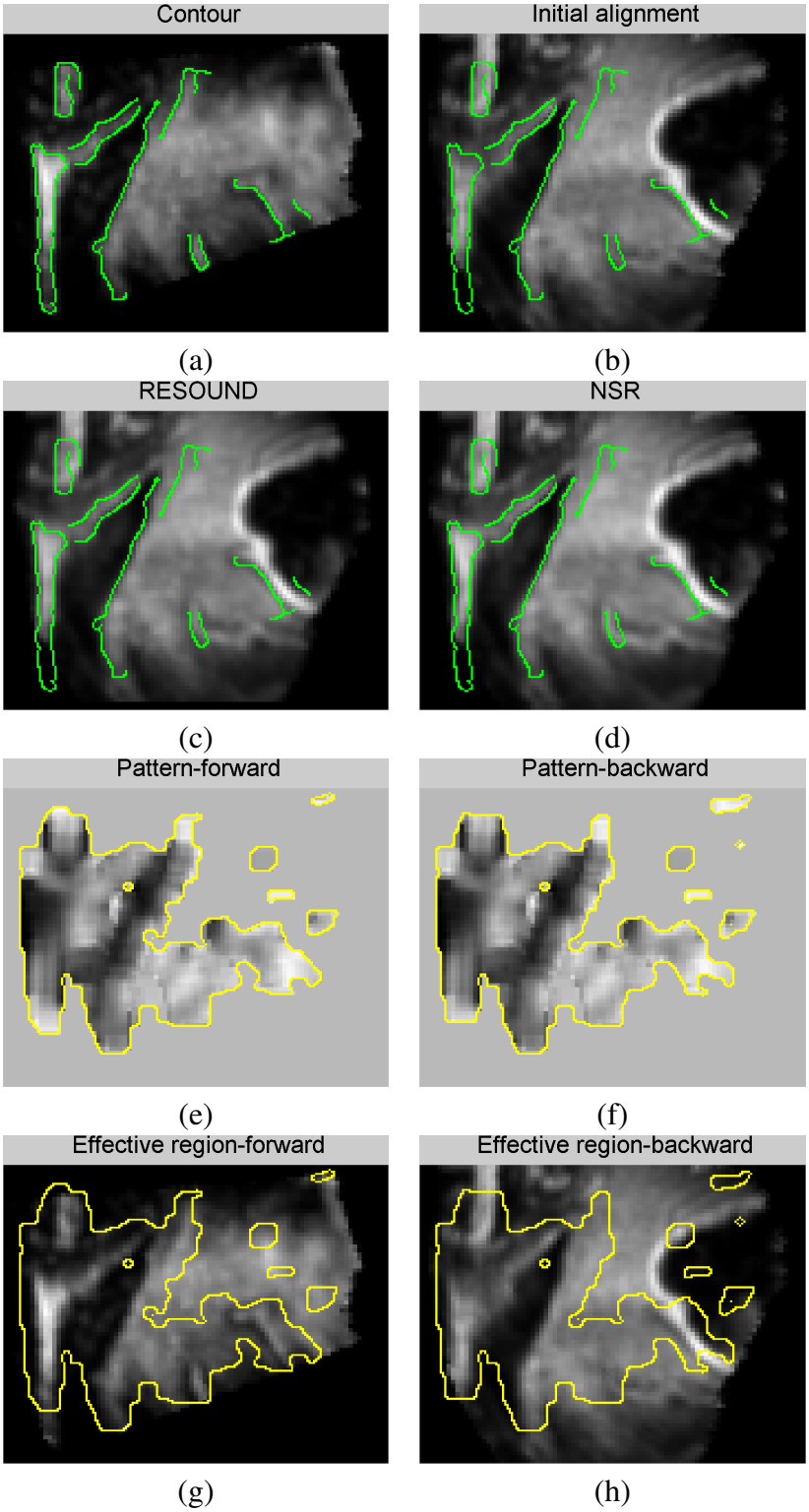

Figure A.9: Registration results of Patient 12. Please refer to the text for details.

Bibliography

[1] H. Rivaz and D. L. Collins, "Near real-time robust non-rigid registration of volumetric ultrasound images for neurosurgery," *Ultrasound in medicine & biology*, vol. 41, no. 2, pp. 574–587, 2015.

[2] D. Fontanarosa, S. van der Meer, J. Bamber, E. Harris, T. O?Shea, and F. Verhaegen, "Review of ultrasound image guidance in external beam radiotherapy: I. treatment planning and inter-fraction motion management," *Physics in medicine and biology*, vol. 60, no. 3, p. R77, 2015.

[3] J. A. Schnabel, M. P. Heinrich, B. W. Papież, and J. M. Brady, "Advances and challenges in deformable image registration: From image fusion to complex motion modelling," *Medical Image Analysis*, 2016.

[4] J.-P. Thirion, "Image matching as a diffusion process: an analogy with maxwell's demons," *Medical image analysis*, vol. 2, no. 3, pp. 243–260, 1998.

[5] D. Rueckert, L. I. Sonoda, C. Hayes, D. L. Hill, M. O. Leach, and D. J. Hawkes, "Non-rigid registration using free-form deformations: application to breast mr images," *IEEE transactions on medical imaging*, vol. 18, no. 8, pp. 712–721, 1999.

[6] M. A. Viergever, J. A. Maintz, S. Klein, K. Murphy, M. Staring, and J. P. Pluim, "A survey of medical image registration–under review," *Medical Image Analysis*, 2016.

[7] G. E. Christensen and H. J. Johnson, "Consistent image registration," *IEEE Transactions on Medical Imaging*, vol. 20, no. 7, pp. 568–582, 2001.

[8] D. Shen and C. Davatzikos, "Hammer: hierarchical attribute matching mechanism for elastic registration," *IEEE Transactions on Medical Imaging*, vol. 21, no. 11, pp. 1421–1439, 2002.

[9] A. Sotiras, C. Davatzikos, and N. Paragios, "Deformable medical image registration: A survey," *Medical Imaging, IEEE Transactions on*, vol. 32, no. 7, pp. 1153–1190, 2013.

[10] F. Maes, A. Collignon, D. Vandermeulen, G. Marchal, and P. Suetens, "Multimodality image registration by maximization of mutual information," *IEEE Transactions on Medical Imaging*, vol. 16, no. 2, pp. 187–198, 1997.

[11] P. Viola and W. M. Wells III, "Alignment by maximization of mutual information," *International journal of computer vision*, vol. 24, no. 2, pp. 137–154, 1997.

[12] R. L. Siegel, K. D. Miller, and A. Jemal, "Cancer statistics, 2015," *CA: a cancer journal for clinicians*, vol. 65, no. 1, pp. 5–29, 2015.

[13] M. Quinn and P. Babb, "Patterns and trends in prostate cancer incidence, survival, prevalence and mortality. part i: international comparisons," *BJU international*, vol. 90, no. 2, pp. 162–173, 2002.

[14] F. Petrelli, I. Vavassori, A. Coinu, K. Borgonovo, E. Sarti, and S. Barni, "Radical prostatectomy or radiotherapy in high-risk prostate cancer: a systematic review and metaanalysis," *Clinical genitourinary cancer*, vol. 12, no. 4, pp. 215–224, 2014.

[15] K. Langen and D. Jones, "Organ motion and its management," *International Journal of Radiation Oncology* Biology* Physics*, vol. 50, no. 1, pp. 265–278, 2001.

[16] M. R. Moman, U. A. van der Heide, A. N. Kotte, R. J. A. van Moorselaar, G. H. Bol, S. P. Franken, and M. van Vulpen, "Long-term experience with transrectal and transperineal implantations of fiducial gold markers in the prostate for position verification in external beam radiotherapy; feasibility, toxicity and quality of life," *Radiotherapy and Oncology*, vol. 96, no. 1, pp. 38–42, 2010.

[17] W. Stummer, U. Pichlmeier, T. Meinel, O. D. Wiestler, F. Zanella, H.-J. Reulen, ALA-Glioma Study Group *et al.*, "Fluorescence-guided surgery with 5-aminolevulinic acid for resection of malignant glioma: a randomised controlled multicentre phase iii trial," *The lancet oncology*, vol. 7, no. 5, pp. 392–401, 2006.

[18] A. Nabavi, P. M. Black, D. T. Gering, C.-F. Westin, V. Mehta, R. S. Pergolizzi Jr, M. Ferrant, S. K. Warfield, N. Hata, R. B. Schwartz *et al.*, "Serial intraoperative magnetic resonance imaging of brain shift," *Neurosurgery*, vol. 48, no. 4, pp. 787–798, 2001.

[19] G. Unsgård, O. Solheim, F. Lindseth, and T. Selbekk, *Intra-operative imaging with 3D ultrasound in neurosurgery*. Springer, 2011.

[20] O. Solheim, T. Selbekk, A. S. Jakola, and G. Unsgård, "Ultrasound-guided operations in unselected high-grade gliomas—overall results, impact of image quality and patient selection," *Acta neurochirurgica*, vol. 152, no. 11, pp. 1873–1886, 2010.

[21] M. A. El Beltagy, M. Aggag, and M. Kamal, "Role of intraoperative ultrasound in resection of pediatric brain tumors," *Child's Nervous System*, vol. 26, no. 9, pp. 1189–1193, 2010.

[22] M. Renovanz, A.-K. Hickmann, C. Henkel, M. Nadji-Ohl, and N. J. Hopf, "Navigated versus non-navigated intraoperative ultrasound: is there any impact on the extent of resection of high-grade gliomas? a retrospective clinical analysis." *Journal of neurological surgery. Part A, Central European neurosurgery*, vol. 75, no. 3, pp. 224–230, 2014.

[23] A. K. Petridis, M. Anokhin, J. Vavruska, M. Mahvash, and M. Scholz, "The value of intraoperative sonography in low grade glioma surgery," *Clinical neurology and neurosurgery*, vol. 131, pp. 64–68, 2015.

[24] J. Coburger, A. Scheuerle, D. R. Thal, J. Engelke, M. Hlavac, C. R. Wirtz, and R. König, "Linear array ultrasound in low-grade glioma surgery: histology-based assessment of accuracy in comparison to conventional intraoperative ultrasound and intraoperative mri," *Acta neurochirurgica*, vol. 157, no. 2, pp. 195–206, 2015.

[25] A. V. Moiyadi and P. Shetty, "Direct navigated 3d ultrasound for resection of brain tumors: a useful tool for intraoperative image guidance," *Neurosurgical Focus*, vol. 40, no. 3, p. E5, 2016.

[26] T. Selbekk, A. S. Jakola, O. Solheim, T. F. Johansen, F. Lindseth, I. Reinertsen, and G. Unsgård, "Ultrasound imaging in neurosurgery: approaches to minimize surgically induced image artefacts for improved resection control," *Acta neurochirurgica*, vol. 155, no. 6, pp. 973–980, 2013.

[27] J. A. Zagzebski, "Essentials of ultrasound physics," 1996.

[28] P. Foroughi, P. Abolmaesumi, and K. Hashtrudi-Zaad, "Intra-subject elastic registration of 3d ultrasound images," *Medical image analysis*, vol. 10, no. 5, pp. 713–725, 2006.

[29] R. J. Schneider, D. P. Perrin, N. V. Vasilyev, G. R. Marx, J. Pedro, and R. D. Howe, "Real-time image-based rigid registration of three-dimensional ultrasound," *Medical image analysis*, vol. 16, no. 2, pp. 402–414, 2012.

[30] I. Reinertsen, F. Lindseth, C. Askeland, D. H. Iversen, and G. Unsgård, "Intra-operative correction of brain-shift," *Acta neurochirurgica*, vol. 156, no. 7, pp. 1301–1310, 2014.

[31] V. Grau, H. Becher, and J. A. Noble, "Registration of multiview real-time 3-d echocardiographic sequences," *IEEE Transactions on Medical Imaging*, vol. 26, no. 9, pp. 1154–1165, 2007.

[32] K. Rajpoot, J. A. Noble, V. Grau, C. Szmigielski, and H. Becher, "Multiview rt3d echocardiography image fusion," in *Functional Imaging and Modeling of the Heart*. Springer, 2009, pp. 134–143.

[33] L. Mercier, D. Araujo, C. Haegelen, R. F. Del Maestro, K. Petrecca, and D. L. Collins, "Registering pre-and postresection 3-dimensional ultrasound for improved visualization of residual brain tumor," *Ultrasound in medicine & biology*, vol. 39, no. 1, pp. 16–29, 2013.

[34] B. Presles, M. Fargier-Voiron, M.-C. Biston, R. Lynch, A. Munoz, H. Liebgott, P. Pommier, S. Rit, and D. Sarrut, "Semiautomatic registration of 3d transabdominal ultrasound images for patient repositioning during postprostatectomy radiotherapy," *Medical physics*, vol. 41, no. 12, p. 122903, 2014.

[35] T. O'Shea, J. Bamber, and E. Harris, "Mo-de-210-05: Improved accuracy of liver feature motion estimation in b-mode ultrasound for image-guided radiation therapy," *Medical physics*, vol. 42, no. 6, pp. 3560–3560, 2015.

[36] J. Banerjee, C. Klink, E. D. Peters, W. J. Niessen, A. Moelker, and T. van Walsum, "Fast and robust 3d ultrasound registration–block and game theoretic matching," *Medical image analysis*, vol. 20, no. 1, pp. 173–183, 2015.

[37] Y. Gao, J. Ma, J. Zhao, J. Tian, and D. Zhang, "A robust and outlier-adaptive method for non-rigid point registration," *Pattern Analysis and Applications*, vol. 17, no. 2, pp. 379–388, 2014.

[38] A. Khamene, D. Zikic, M. Diallo, T. Boettger, and E. Rietzel, "A novel intensity similarity metric with soft spatial constraint for a deformable image registration problem in radiation therapy," in *Medical Image Computing and Computer-Assisted Intervention–MICCAI 2009*. Springer, 2009, pp. 828–836.

[39] H. Zhou and H. Rivaz, "Registration of pre-and post-resection ultrasound volumes with non-corresponding regions in neurosurgery," *IEEE Journal of Biomedical and Health Informatics*, vol. PP, no. 99, pp. 1–1, 2016.

[40] E. Malis, "Improving vision-based control using efficient second-order minimization techniques," in *ICRA'04. 2004 IEEE International Conference on Robotics and Automation*, vol. 2. IEEE, 2004, pp. 1843–1848.

[41] H. Zhou and H. Rivaz, "Robust deformable registration of pre-and post-resection ultrasound volumes for visualization of residual tumor in neurosurgery," in *Engineering in*

Medicine and Biology Society (EMBC), 2015 37th Annual International Conference of the IEEE. IEEE, 2015, pp. 141–144.

[42] M. P. Heinrich, M. Jenkinson, M. Bhushan, T. Matin, F. V. Gleeson, M. Brady, and J. A. Schnabel, "Mind: Modality independent neighbourhood descriptor for multi-modal deformable registration," *Medical Image Analysis*, vol. 16, no. 7, pp. 1423–1435, 2012.

[43] M. Chen, W. Lu, Q. Chen, K. J. Ruchala, and G. H. Olivera, "A simple fixed-point approach to invert a deformation field," *Medical physics*, vol. 35, no. 1, pp. 81–88, 2008.

[44] H. Rivaz, S. J.-S. Chen, and D. L. Collins, "Automatic deformable mr-ultrasound registration for image-guided neurosurgery," *IEEE Transactions on Medical Imaging*, vol. 34, no. 2, pp. 366–380, 2015.

[45] E. Malis, "Vision-based estimation and robot control," Ph.D. dissertation, Université Nice Sophia Antipolis, 2008.

[46] L. Mercier, R. F. Del Maestro, K. Petrecca, D. Araujo, C. Haegelen, and D. L. Collins, "Online database of clinical mr and ultrasound images of brain tumors," *Medical physics*, vol. 39, no. 6, pp. 3253–3261, 2012.

[47] P. Jannin, J. M. Fitzpatrick, D. Hawkes, X. Pennec, R. Shahidi, and M. Vannier, "Validation of medical image processing in image-guided therapy." *IEEE Transactions on Medical Imaging*, vol. 21, no. 12, pp. 1445–1449, 2002.

[48] M. Van Herk, "Errors and margins in radiotherapy," in *Seminars in radiation oncology*, vol. 14, no. 1. Elsevier, 2004, pp. 52–64.

[49] H. A. McNair, V. N. Hansen, C. C. Parker, P. M. Evans, A. Norman, E. Miles, E. J. Harris, L. Del-Acroix, E. Smith, R. Keane *et al.*, "A comparison of the use of bony anatomy and internal markers for offline verification and an evaluation of the potential benefit of online and offline verification protocols for prostate radiotherapy," *International Journal of Radiation Oncology* Biology* Physics*, vol. 71, no. 1, pp. 41–50, 2008.

[50] M. Lachaine and T. Falco, "Intrafractional prostate motion management with the clarity autoscan system," *Med. Phys. Int*, vol. 1, no. 1, pp. 72–80, 2013.

[51] J. A. Molloy, G. Chan, A. Markovic, S. McNeeley, D. Pfeiffer, B. Salter, and W. A. Tome, "Quality assurance of us-guided external beam radiotherapy for prostate cancer: Report of aapm task group 154," *Medical physics*, vol. 38, no. 2, pp. 857–871, 2011.

[52] M. Fargier-Voiron, B. Presles, P. Pommier, A. Munoz, S. Rit, D. Sarrut, and M.-C. Biston, "Evaluation of a new transperineal ultrasound probe for inter-fraction image-guidance for definitive and post-operative prostate cancer radiotherapy," *Physica Medica*, vol. 32, no. 3, pp. 499–505, 2016.